A novel iPSC model of Bryant-Li-Bhoj neurodevelopmental syndrome demonstrates the role of histone H3.3 in neuronal differentiation and maturation

Annabel K. Sangree[1,2]*, Rajesh Angireddy[1]*, Laura M. Bryant[1,3], Dana E. Layo-Carris[1], Emily E. Lubin[1,2], Xiao Min Wang[1], Kelly J. Clark[1,2], Emily E. Durham[1], Elizabeth J. Bhoj[1,2]

Author affiliations:

1. Department of Human Genetics, Children's Hospital of Philadelphia, Philadelphia, PA, USA
2. Perelman School of Medicine, University of Pennsylvania, Philadelphia, PA, USA
3. Steve and Cindy Rasmussen Institute for Genomic Medicine, Nationwide Children's Hospital, Columbus, OH, USA

* Equal contributors

Corresponding author contact: bhoje@chop.edu

ABSTRACT

Background

Bryant-Li-Bhoj neurodevelopmental syndrome (BLBS) is neurogenetic disorder caused by variants in *H3-3A* and *H3-3B,* the two genes that encode the histone H3.3 protein. Ninety-nine percent of individuals with BLBS show developmental delay/intellectual disability, but the mechanism by which variants in H3.3 result in these phenotypes is not yet understood. As a result, only palliative interventions are available to individuals living with BLBS.

Methods

Here, we investigate how one BLBS-causative variant, *H3-3B* p.Leu48Arg (L48R), affects neurodevelopment using an induced pluripotent stem cell (iPSC) model differentiated to 2D neural progenitor cells (NPCs), 2D forebrain neurons (FBNs), and 3D dorsal forebrain organoids (DFBOs). We employ a multi-omic approach in the 2D models to quantify the resulting changes in gene expression and chromatin accessibility. We used immunofluorescence (IF) staining to define the identities of cells in the 3D DFBOs.

Results

In the 2D systems, we found dysregulation of both gene expression and chromatin accessibility of genes important for neuronal fate, maturation, and function in H3.3 L48R compared to control. Our work in 3D organoids corroborates these findings, demonstrating altered proportions of radial glia and mature neuronal cells.

Conclusions

These data provide the first mechanistic insights into the pathogenesis of BLBS from a human-derived model of neurodevelopment, which suggest that the L48R increases *H3-3B* expression, resulting in the hyper-deposition of H3.3 into the nucleosome which underlies changes in gene expression and chromatin accessibility. Functionally, this causes dysregulation of cell adhesion, neurotransmission, and the balance between excitatory and inhibitory signaling. These results are a crucial step towards preclinical development and testing of targeted therapies for this and related disorders.

Keywords: Histone H3.3, Mendelian neurodevelopmental disorder, chromatin, iPSC, brain organoid, multi-omic, translational neurogenetics

BACKGROUND

Neurodevelopmental disorders (NDDs) affect 1-8% of the population and are often the result of aberrant components of epigenetic machinery following a genetic insult in the earliest stages of neurodevelopment[1]. Mendelian disorders of epigenetic machinery (MDEMs), caused by germline variants in 85 genes encoding histone writers, readers, erasers, and chaperones, are associated with a wide spectrum of NDDs, highlighting the brain's vulnerability to transcriptional dysregulation[2]. Recently, variants in histones themselves emerged as causative in NDDs with the identification of *de novo* germline variants in the H4 encoding gene cluster[3,4] and the H3.3-encoding genes *H3-3A* and *H3-3B*[5–7].

59 Bryant-Li-Bhoj neurodevelopmental syndrome (BLBS, OMIM #619720, #619721) is an NDD
60 caused by heterozygous germline variants in *H3-3A* or *H3-3B*. Variants underlying BLBS occur
61 throughout the coding sequences of *H3-3A* and *H3-3B* and are typically observed in just one
62 individual[5,8]. Phenotypically, affected individuals present almost universally with neurologic and
63 craniofacial features. The most prevalent neurologic feature is developmental delay/intellectual
64 disability, which impacts 99% of published individuals with 51% of individuals exhibiting delayed
65 or no attainment of sitting, 79% of individuals exhibiting delayed or no attainment of independent
66 walking, and more than 40% of individuals not yet having attained their first word at >20
67 months[8]. From a neuroradiological standpoint, individuals most commonly have delayed
68 myelination or hypomyelination, dysgenesis of the corpus callosum, and/or dilated ventricles[9].
69 As some individuals age, they develop an abnormal gait or progressive gait ataxia
70 phenotype[5,7,8]. While no targeted therapeutics are available at this time, these
71 neurodegenerative phenotypes suggest that BLBS could be amenable to therapeutic
72 intervention to halt disease progression.

73 A mechanistic link has not yet been established between the physiologic function of H3.3 and its
74 dysregulation in BLBS. H3.3 is a replication-independent histone that packages DNA and
75 regulates gene expression. It is preferentially deposited by the chaperones DAXX or HIRA at
76 enhancers, promoters, and gene bodies[10–18]. Because its deposition is not coupled to the cell
77 cycle, H3.3 plays a critical epigenetic role in post-mitotic neuronal populations in the brain,
78 especially in regulating transcription during learning and memory[19]. During early
79 neurodevelopment in mice, H3.3 accounts for an estimated 31% of the total H3 pool[20]. Because
80 almost all neural proliferation occurs prenatally, replication-coupled deposition of H3-class
81 histones H3.1 and H3.2 stops during gestation, meaning H3.3 accumulates with age and
82 becomes the highly dominant form of H3 (>93%) in adult neurons[21]. Throughout all stages of

83 neurodevelopment, H3.3 plays a crucial role in establishing chromatin landscapes,
84 transcriptome, molecular identity, and axon connectivity in newly post-mitotic neurons[10].
85
86 The role of H3.3 in disease was first appreciated in cancer through the discovery of somatic
87 'oncohistone' mutations[22–24]. In *H3-3A*, p.Gly34Arg/Val mutations drive pediatric diffuse
88 hemispheric glioma[25], p.Lys27Met mutations drive diffuse midline gliomas[26,27], and
89 p.Gly34Trp/Leu mutations drive giant cell tumor of bone[28]. Distinct *H3-3B* p.Lys36Met mutations
90 drive chondroblastoma[28]. While extensive work has been done to elucidate the mechanism of
91 these somatic oncohistone mutations, we still have a limited understanding of how germline
92 missense perturbation of H3.3 affects neurodevelopment.
93
94 Past studies into the effects of germline missense perturbation of H3.3 utilized cells from
95 affected individuals, overexpression systems, and mouse models[5,6,29]. Dermal fibroblasts from
96 affected individuals hyper-proliferate compared to age- and sex-matched controls[5]. *In silico*
97 predictions of the effects of these variants on histone post translational modifications (hPTMs)
98 suggest that certain mutants alter phosphorylation, glycosylation, methylation, acetylation, and
99 ubiquitination *in cis*[7]. In mice, three different variants at the same residue (p.Gly34Arg/Val/Trp)
100 cause distinct developmental defects. p.Gly34Arg mice have severe neurodegeneration,
101 p.Gly34Trp mice have obesity and bladder obstructions, and p.Gly34Val mice have intermediate
102 phenotypes[29]. These models capture the same phenotypic heterogeneity recently reported
103 amongst individuals living with BLBS, including those who share the same causative nucleotide
104 level substitution[8]. These studies highlight the importance of studying individual variants, as
105 both affected individuals and models display variable phenotypes. Moreover, there is a gap in
106 knowledge as to how these variants affect human development in affected organs, most
107 strikingly the brain, highlighting the necessity of interrogating the effect of BLBS-causing
108 variants in human iPSCs.

109 Here, we profile the transcriptomes and chromatin accessibility changes induced by one variant
110 observed in our cohort, *H3-3B* p.Leu48Arg (L48R). This variant lies just beyond the N terminal
111 tail, in the histone core[8], a region of H3.3 that is less well studied in the context of disease. The
112 individual harboring the L48R variant presents with neurologic features that include
113 developmental delay/intellectual disability, microcephaly, hypomyelination, hypotonia that
114 transitioned to hypertonia, and seizures.
115
116 To elucidate how this variant affects neurodevelopment, we differentiated isogenic control and
117 L48R iPSCs into 2D neural progenitor cells (NPCs) and 2D forebrain neurons (FBNs). We
118 employed a multi-omic approach in our 2D system and identified critical genes and pathways
119 that affected NPC differentiation into neurons and glia. We validated our findings from 2D
120 cultures with 3D organoid models of the brain, which faithfully recapitulate developing
121 neuroectoderm with the radial organization of NPC cells into structures that recapitulate the
122 ventricular zone (VZ), subventricular zone (SVZ), and cortical plate (CP)[30]. This innovative
123 approach employing both 2D and 3D models elucidated global dysregulation in gene expression
124 and chromatin accessibility of genes important for cell adhesion, axon development, and
125 neurotransmission. Taken together, we find that H3.3 L48R perturbs neurodifferentiation and
126 neuronal maturation in this iPSC model of brain development. Our results lay the foundation for
127 future studies on BLBS and therapeutic interventions.
128
129 **RESULTS**
130 **L48R variant affects iPSC differentiation into 2D neural progenitor cells (NPCs) and 2D**
131 **forebrain neurons (FBNs)**
132 We introduced the heterozygous c.146T>G *H3-3B* Leu48Arg (L48R) variant into CHOPWT14
133 iPSCs (from a Hispanic 46XX donor) using CRISPR/Cas9 homology directed repair (HDR)[31]
134 followed by single cell clone selection and validation by Sanger sequencing (Fig. 1A, Fig. S1A-

135 B). To validate their pluripotency, we performed RT-qPCR for *OCT4* and *NANOG* in these
136 iPSCs (Fig. 1B). We did not observe significant changes in the expression of these markers
137 between L48R and control cells, confirming that this variant did not have a large impact on the
138 identity of iPSCs.
139
140 To begin delineating the effects of the H3.3 L48R variant on brain development and neuronal
141 function, we differentiated L48R and isogenic control iPSCs into NPCs using a dual SMAD
142 inhibition protocol[46]. We found that the L48R NPCs had lower expression of the NPC markers
143 *NES* (encodes Nestin) and *SOX1* than the isogenic control (Fig. 1C), indicating that this variant
144 affects early neuronal differentiation. Next, we differentiated the NPCs to FBNs using a protocol
145 that generates a mixed population of 90% forebrain-type neurons (MAP2+ and TUJ1+) with
146 about 10% glial cells (GFAP+) (Stem Cell Technologies #08600, #08605). We immunostained
147 FBNs at day 20 of maturation for the neuronal marker TUJ1 and glial marker GFAP and
148 observed a larger glial population in the L48R cells (Fig. S1C, D). Further staining indicated a
149 loss of MAP2+ neuronal extensions and decreased intensity of the glutamate transporter
150 VGLUT1 in the L48R FBNs compared to isogenic controls (Fig. 1D, E). We did not find a
151 difference between *MAP2* mRNA expression measured via RT-qPCR between the two
152 conditions (Fig. S1E), but we found a significant increase in *GFAP* mRNA levels in L48R FBNs
153 compared to isogenic controls (Fig. 1F). Taken together, we observed disruptions in the
154 differentiation of L48R iPSCs to NPCs, which impacted subsequent differentiation into FBNs, as
155 measured by decreased MAP2 staining and increased GFAP expression.
156
157 **Transcriptomic changes in L48R progenitor cells affect differentiation into 2D FBNs**
158 We performed bulk RNA-seq of iPSCs, NPCs, and FBNs to understand the global
159 transcriptomic changes induced by L48R at various stages of differentiation (Supplementary File
160 1). Principal component analysis (PCA) on the different cell types identified three distinct

161 clusters based on cell identity (Fig. S2A). We identified 96 genes with significantly altered
162 expression ($p \leq 0.05$) in L48R iPSCs compared to the isogenic controls (Fig. 2A). Using an
163 additional threshold of absolute value log2-fold change (LFC) ≥ 1, 37 genes were significantly
164 upregulated, while 20 were downregulated. Using a gene ontology (GO) analysis, we found no
165 significantly altered pathways in the L48R iPSCs compared to isogenic controls, but did identify
166 the upregulation of *CDKL5* (LFC = 1.46, adjusted p-value = 6.36E-09) and *SCML2 (*LFC = 1.04,
167 adjusted p-value = 4.98-E07), both of which are genes important for cell cycle progression and
168 differentiation[47,48] (Table 1). Table 1 contains the function of these, and other genes discussed
169 in this work. These transcriptomic results indicate that L48R might impact the ability of iPSCs to
170 proliferate and differentiate into NPCs.
171
172 Nearly twice as many genes were dysregulated in L48R NPCs. Bulk RNA-seq on NPCs
173 identified 139 differentially expressed genes in L48R NPCs ($p \leq 0.05$) compared to control
174 NPCs. 53 genes were upregulated (LFC ≥ 1) and 27 downregulated (LFC ≤ -1) (Fig. 2B). GO
175 analysis for all differentially expressed genes indicate processes like cell migration and
176 establishment of synapses are affected, including pathways involved in cell adhesion, synapse
177 organization, regulation of axonogenesis, neuron projection extension, and regulation of axon
178 extension (Fig. 2C, Table 1). We focused on genes comprising the cell adhesion and
179 axonogenesis pathways (Fig. 2D). Most genes related to these processes were upregulated in
180 L48R NPCs compared to controls, including several protocadherin-encoding genes, which
181 mediate neurite repulsion[49]. *CDH4* and *WNT7A* were downregulated, indicating an imbalance
182 in cell adhesion and axon development cues (Table 1).
183
184 When L48R NPCs were converted to FBNs, we observe massive transcript-level dysregulation
185 (773 genes up, 965 down) (Fig. 2E). *EGR1, FOSL1, JUNB,* and *NPAS4,* immediate early genes
186 which mediate genetic responses to environmental cues[50], were downregulated (Fig. 2E, Table

187 1). GO analysis identified the upregulation of terms related to synapse organization and activity,
188 neurotransmitter uptake, and nervous system development (Fig. S2B). It also identified terms
189 related to G/M cell cycle phase transition and mitotic cell cycle phase transition, which are
190 notable given that neurons are post-mitotic (Fig. S2B). Because these terms were enriched,
191 and L48R FBNs had an increase in GFAP staining, we specifically queried the expression of
192 astrocyte genes. We found that astrocyte-associated genes like *AQP4*, *SLC1A3,* and *SLC6A11*
193 are upregulated in L48R FBNs, suggesting that our mixed population of cells is skewing towards
194 proliferating astrocytes, as opposed to post-mitotic neurons (Fig. S2C). BrdU staining revealed
195 an increased staining indicative of proliferation in the L48R cells compared to controls following
196 FBN differentiation (Fig. S2D), further supporting that differentiation of L48R cells did not result
197 in the expected ratio of 90% neurons and 10% glia. When we analyzed the GO terms for down-
198 regulated genes in FBNs, we observed terms like wound healing, regulation of apoptotic
199 signaling pathway, and cellular response to external stimulus (Fig. S2E). Given the
200 dysregulation of fundamental pathways that we observed in NPCs and the downregulation of
201 immediate early genes, it is likely that the widespread dysregulation observed in the FBNs is
202 secondary to these primary deficits.
203
204 To identify causative genes that might affect the overall differentiation of L48R cells, we looked
205 for commonly dysregulated genes at the iPSC, NPC, and FBN stage (Fig. 2F). Two genes were
206 commonly downregulated, and 13 were upregulated in all cell types (Table 2). Restricting the
207 analysis to genes commonly dysregulated at the neuronal NPC and FBN stages, we identified
208 29 genes that were upregulated in both NPCs and FBNS, and 8 that were downregulated (Table
209 3). These genes were implicated in cell adhesion, a crucial process in neurodevelopment that
210 allows for appropriate circuit formation[51].
211

212 **L48R variant increases its own gene expression and has increased protein deposition in**
213 **2D neuronal cell types**
214 Because histones orchestrate chromatin compaction, their deposition in the nucleus affects both
215 genome organization and gene expression. We posited that differential H3.3 deposition
216 between L48R and control cells might underly some of the gene expression changes we
217 observe. In addition to the gene expression changes reported above, we directly queried the
218 altered expression of *H3-3A* and *H3-3B* in cells harboring the L48R variant. Notably, expression
219 of *H3-3B* was significantly upregulated in NPCs (adjusted p-value = 1.58E-9), while *H3-3A*
220 expression was not significantly affected (adjusted p-value = 0.99) (Fig. S3A). We first validated
221 this RNA-seq result, finding that *H3-3B* mRNA levels are upregulated in NPCs, and
222 subsequently observed the same effect in FBNs (Fig. S3B). When we performed a subcellular
223 fractionation in NPCs, we found that H3.3 levels were slightly higher in chromatin and lower in
224 the cytoplasm as compared to controls (Fig. S3C-D). These changes in localization could
225 suggest that the L48R variant affects import of newly translated H3.3 into the nucleus or its
226 incorporation into chromatin. We next stained FBNs for H3.3 to understand the deposition of
227 H3.3 in these post-mitotic cells and quantified the corrected total cellular fluorescence of
228 H3.3/DAPI (Fig. S3E). We observed a significant increase in this metric in L48R cells compared
229 to control, suggesting that H3.3 is hyper-deposited.
230
231 **L48R variant alters chromatin accessibility and the occupancy of transcription factors**
232 **important for neuronal development in 2D models**
233 To understand how this change in deposition affected global chromatin accessibility, we
234 performed Assay for Transposase-Accessible Chromatin with sequencing (ATAC-seq) in two
235 biological replicates of L48R NPCs and isogenic controls. Using DiffBind[43], we identified 350
236 differentially accessible sites (FDR ≤0.05, p ≤ 0.01), which were most commonly within 1kb of a
237 promoter (40.86%) and in distal intergenic regions (21.43%) (Fig. 3A, Supplementary File 2). Of

238 these 350 regions, 253 were significantly more open (fold-change ≥ 1) and 97 regions were
239 significantly less open (fold-change ≤ -1) in the L48R NPCs compared to isogenic controls (Fig.
240 3B). To understand the biological pathways most affected by these chromatin accessibility
241 changes, we performed a GO analysis using all 350 sites. The most common terms were
242 related to regulating neuronal development, axonogenesis, and cell growth (Fig. 3C). *PLXNA3*,
243 a gene important for axon extension[52,53], had significantly more open chromatin in the L48R
244 NPCs compared to controls (Fig. 3D). *RBFOX1*, an RNA-binding protein that regulates neuronal
245 splicing and is implicated in a range of NDDs[54] had regions of more compact chromatin
246 compared to control (Fig. S3E). Taken together, we found changes in H3.3 deposition in
247 neuronal cell types harboring the L48R variant. The resulting aberrant chromatin accessibility
248 occurred at sites important for early neural development (*RBFOX1*) as well as later stages of
249 axon and synapse development (*PLXNA3*), suggesting that some genomic regions may be
250 improperly poised for transcription in cells that harbor the L48R variant.
251
252 Next, we interrogated how changes in chromatin accessibility affected transcription factor (TF)
253 occupancy. Using ATACseqTFEA[55], we performed a TF enrichment analysis and identified 64
254 TFs predicted to have differential occupancy between L48R and control. This analysis
255 generates enrichment scores; positive scores indicates that the motif(s) for a TF are enriched in
256 L48R cells, and negative scores indicate that the motif(s) are depleted in L48R cells. Significant
257 factors were called with an adjusted p-value ≤ 0.05. Of these factors, *ZNF614*, *PBX1,* and *ARX1*
258 had the greatest enrichment scores (increased occupancy in L48R), while *TP63* and *EMX2* had
259 the most negative scores (decreased occupancy in L48R) (Fig. 3E). Increased occupancy of
260 these TFs supports our previous data that transcription is altered, with a specific effect on
261 neurotransmission. Meanwhile, the factors that were depleted in L48R support the
262 transcriptomic data that the L48R variant impairs NPC differentiation.
263

264 We performed a GO analysis of all factors with changes in occupancy and performed a
265 dimensional reduction of these terms using REVIGO[36] (Fig. 3F). The terms clustered into four
266 groups represented by the terms: pattern specification process (cluster 1), mononuclear cell
267 differentiation (cluster 2), regulation of epithelial cell differentiation (cluster 3), and neural
268 precursor cell proliferation (cluster 4) (Fig. 3F). Every cluster contains TFs important for fate
269 specification in the developing nervous system. The most affected terms are important for
270 transcription of genes required for neural precursor cell proliferation, stem cell differentiation and
271 fate commitment, and forebrain development. To understand if altered TF occupancy might
272 account for changes in gene expression, we used TFLink[56] to find the targets of ZNF614, PBX1,
273 and ARX (increased occupancy) as well as TP63 and EMX2 (decreased occupancy), and
274 looked for changes in gene expression in our NPC RNA-seq dataset. The TFs with the greatest
275 number of targets affected in this dataset were *PBX1* (12 up, 5 down) and *TP63* (32 up, 19
276 down) (Table 4). *DPP6*, *GABRG3*, *GABRA5, CDH4, PCDHGA3, WNT7A*, and *PLXNA3*, genes
277 with the largest differences in expression in L48R NPCs as compared to control, are all
278 predicted targets of p63 regulation. While validation is required to show changes in
279 binding/activity of these factors, these data support that the L48R variant affects TF binding by
280 driving changes in chromatin accessibility, resulting in aberrant expression of genes required for
281 NPC differentiation into mature neurons.
282
283 **Chromatin accessibility changes in L48R NPCs affect expression of genes important for**
284 **cell adhesion and neurotransmission in 2D model**
285 We next queried the overlap between ATAC-seq and RNA-seq datasets. First, we identified six
286 genes that were down in both datasets ($p \leq 0.05$, LFC ≤ -1) (Fig. 4A). *CDH4* was the most
287 downregulated gene across these datasets (Fig. 4B, Table 1). We performed RT-qPCR gene
288 expression analysis in iPSCs, NPCs, and FBNs to validate these results, and to understand
289 *CDH4*'s expression during both development and maturation. In isogenic controls, *CDH4*

290 expression increased as the iPSCs were differentiated to NPCs and FBNs, but when L48R
291 iPSCs were differentiated to NPCs and FBNs, *CDH4* had nearly undetectable levels (Fig. 4C).
292
293 Then, we identified 27 genes that were significantly upregulated in both datasets ($p \leq 0.05$, LFC
294 ≥ 1). Notable genes include *GABRG3* and *DPP6*, two genes involved in neurotransmission (Fig.
295 3D, Table 1). *GABRG3* had more open chromatin at its promoter (Fig. 3E) and its expression
296 increased as iPSCs were differentiated to NPCs and FBNs, with a significantly greater increase
297 in L48R cells compared to control (Fig. 3F). A related gene, *GABRA5,* was also significantly up
298 in both datasets (Fig. 3D, Fig. S3F). Further, DiffBind called eight different regions of *DPP6*
299 more accessible in L48R NPCs: 1 exonic, 4 intronic, and 3 within 1kb of its promoter (Fig. 3G).
300 When we analyzed the expression of *DPP6* in iPSCs, NPCs, and FBNs, we observed a 20,000-
301 100,000-fold induction in L48R NPCs and FBNs (Fig. 3J). Taken together, our ATAC-seq and
302 RNA-seq identified a set of genes important for neurotransmission, neuronal identity, and cell
303 cycle progression with expression and chromatin architecture that are perturbed by the L48R
304 variant in NPCs. The changes in *H3-3B* expression and H3.3 deposition, coupled with altered
305 TF occupancy, suggest that L48R drives altered chromatin accessibility, resulting in abnormal
306 gene expression and subsequently affecting NPC differentiation into neurons and glia.
307
308 **L48R variant affects radial glia and alters neuronal maturation in 3D dorsal forebrain**
309 **organoids**
310 Using an orthogonal model system to further analyze the neurodevelopmental consequences of
311 the L48R variant, we utilized 3D dorsal forebrain organoids (DFBOs) to understand cortical
312 development, neuronal maturation, and organization. To study the effects of the L48R variant on
313 early brain development, we converted isogenic control and L48R 2D iPSCs into 3D DFBOs[45]
314 and analyzed them at different time points (Fig. S4A). DFBOs were collected at day 25 (D25) to
315 analyze the neuroepithelial expansion (NE) and at day 62 (D62) to analyze maturation. We

316 analyzed organoid size across stages of development and observed that L48R organoids were
317 larger at day 25 compared to isogenic controls, but this difference was not observable at later
318 time points (Fig. 4A). L48R DFBOs at D62 had fewer NE buds at their edges than isogenic
319 controls (Fig. S4B).
320
321 At D25 and D62, we observed autonomously organized radial glia in both sets of organoids by
322 staining them with SOX2 (Fig. 5B). While there was no difference in SOX2 staining at D25 (Fig
323 5B, C), L48R DFBOs had significantly less expression of this marker at D62 (Fig. 5B, C). We
324 also stained these organoids with PAX6, another radial glia marker, at D62 and observed a
325 decrease in this marker (Fig. S4C). Next, we stained organoids with CTIP2, a marker of
326 intermediate progenitor neurons. While not significant, we observed that L48R DFBOs had more
327 CTIP-positive cells at both time points (Fig. S4D). During neurodevelopment, radial glia
328 undergo both symmetric division, allowing for self-renewal, and asymmetric division, which
329 produce intermediate progenitor neurons[57] further supporting that the pool of radial glia are
330 being depleted through a skewing towards asymmetric division, leading to increased progenitors
331 committed to a neuronal fate. L48R DFBOs had decreased TUJ1 staining at D25, but this
332 difference was not present at D62 (Fig. 5B,C). This may suggest that, while increased CTIP2+
333 intermediate progenitor cells are available, they are less able to mature into TUJ1+ neurons
334 within this D25 to D62 timeframe. Since we observed dysregulation in the radial glia population,
335 we stained D25 and D62 organoids with SOX2 and the cell proliferation marker Ki67. We
336 observed fewer Ki67-positive cells at both stages, indicating a defect to the expanding NE (Fig.
337 5D). These results indicate that L48R radial glia may have a functional deficit that interferes with
338 the self-renewing symmetric division of these cells, leading to an expansion of the asymmetric-
339 division-derived intermediate progenitor cell population when compared to WT. This
340 proliferation defect likely explains our earlier observations that L48R organoids have fewer
341 progenitor cells as they mature (Fig. 5B, C).

342

343 To understand how the L48R variant affects neuronal maturation, we stained organoids with
344 mature neuronal marker MAP2, which stains the dendrites of mature post-mitotic neurons. We
345 stained DFBOs collected at D62 with MAP2 and observed significantly lower levels in the L48R
346 DFBOs (Fig. 6A). These results also validate our findings in 2D FBNs (Fig. 1D). To this point,
347 we identified that L48R DFBOs had fewer proliferating radial glia, an expanded pool of
348 intermediate progenitors, and less mature TUJ1+ neurons at D62. However, from these
349 experiments alone, it is not clear whether these differences in cellular composition affected the
350 function of these organoids. To begin to answer this question, we looked at the expression of
351 GABA, as our sequencing experiments elucidated an increased expression of GABA receptors
352 *GABRG3* and *GABRA5*. We stained for GABA in D62 DFBOs and observed more GABA
353 staining in the L48R condition (Fig. 6B). Further, we observed significantly higher mRNA
354 expression of *GABRG3* in L48R DFBOs (Fig. 6C), validating our sequencing results in an
355 orthogonal model. Taken together, our work in DFBOs indicates that the L48R variant affect
356 both symmetric radial glial proliferation and asymmetric radial glia division, ultimately leading to
357 defects in neuronal maturation. Further, these results suggest that the L48R mutation altered
358 neuronal subtypes, potentially leading to an imbalance of excitatory/inhibitory signaling.
359

360 **DISCUSSION**

361 BLBS is a rare Mendelian syndrome with a mixed neurodevelopmental/neurodegenerative
362 phenotype for which only palliative interventions are currently available. Prior work in patient-
363 derived dermal fibroblasts, zebrafish, and mice have facilitated insights into the pathogenic
364 mechanism of this neurogenetic disorder[5,7]. However, until this work, the neurologic phenotype
365 of BLBS had never been interrogated in a human model of neurodevelopment. In the first
366 reported human iPSC-derived model of BLBS, we show that one BLBS causative variant, *H3-3B*
367 p.L48R, impairs neuronal differentiation and maturation in both 2D iPSC and 3D organoid

368 systems. We find that the identity of cells at the iPSC stage is largely unaffected by the L48R
369 variant (Fig. 1B), but that there are changes in cell cycle regulators and cell adhesion molecules
370 that affect differentiation to NPCs (Fig. 2A, Fig. S2B). NPCs have decreased expression of fate
371 markers like *NES* and *SOX1* (Fig. 1C), and factors important for differentiation including *CDH4,*
372 *WNT7A* and *L1CAM* (Fig. 2B-D). L48R FBNs express reduced MAP2 (Fig 1D, E) and
373 immediate early genes (Fig 2E) and increased astrocyte markers like *GFAP* and *AQP4* (Fig.
374 S2D). These results indicate that L48R specifically affects differentiation from iPSCs to NPCs
375 and FBNs, and results in dysfunctional neuronal populations. Disruption of these crucial
376 processes would have significant neurodevelopmental consequences, which may begin to
377 provide insight into the near-universal neurologic phenotype associated with BLBS. Further,
378 myelin-related anomalies account for 46% of findings on MRIs[9]. Clinical evidence coupled with
379 FBN data indicating increased astrocytic markers necessitate future work to understand if the
380 L48R variant skews progenitors towards a glial fate, or if glia outcompete neurons that are
381 affected by the variant.
382
383 To further interrogate the drivers of these changes in gene expression in NPCs and FBNs
384 harboring the L48R variant, we investigated how the expression of *H3-3B* itself was affected
385 and found that *H3-3B* expression was upregulated in both L48R NPCs and FBNs. There was
386 also increased H3.3 deposition in L48R FBNs (Fig. S3A-D). This variant's effect on its own gene
387 expression suggests that it might be acting through a gain of function mechanisn[58], meaning
388 that gene disruption therapies could be a viable therapeutic option for individuals with BLBS.
389 Next, we defined the chromatin landscape of L48R NPCs using ATAC-seq and identified
390 changes in chromatin accessibility at genomic regions important for axon guidance, neuron
391 projection, and synapse organization (Fig. 3C, D). We also found changes in the occupancy of
392 TFs that regulate processes like axon guidance and GABAergic neuron differentiation (Fig. 3E,
393 F). We were able to broadly define the chromatin landscape of L48R NPCs using ATAC-seq.

394 However, chromatin immunoprecipitation with sequencing (ChIP-seq) for H3.3 and the
395 distribution of active/repressive hPTMs like H3K4me3, H3K36me3, H3K27ac and H3K27me3
396 will provide more granular detail as to the mechanism underlying the changes in chromatin
397 states. These experiments could also contribute to our understanding of why germline mutations
398 in H3.3 cause BLBS, but somatic mutations lead to cancer. H3.3 p.Lys27Met causes a global
399 reduction in H3K27me2/3[59], while H3.3 p.Gly34 variants alter H3K36 and H3K27 methylation *in*
400 *cis*[60]. Given that oncohistone mutations are restricted to the H3.3 tail[24], while BLBS mutations
401 occur throughout the protein, it is likely that the effect of BLBS on hPTMs is more subtle than
402 that of p.Lys27 and p.Gly34 mutations. ChIP-seq for H3.3 would also indicate changes in
403 chromatin accessibility and gene expression at the sites were due directly to altered H3.3
404 deposition.
405
406 When integrating our multi-omic data, we found that the RNA- and ATAC-seq datasets
407 overlapped at a few key sites, and generally had more upregulated genes/open chromatin in
408 L48R NPCs compared to isogenic controls (Fig. 4D). Many genes were related to key
409 neurodevelopmental processes, such as cell adhesion and neurotransmission, which may
410 provide actionable or targetable insights into the pathogenesis of BLBS. The consistent
411 downregulation of *CDH4*, a gene that encodes a cadherin fundamental for cell-cell interactions
412 in the central nervous system, might be one of the first causes of differentiation deficits in L48R
413 cells. The upregulation of *DPP6* and GABA receptors *GABRG3* and *GABRA5* suggest that
414 L48R cells have impaired neurotransmission with decreased neuronal activity, a phenomenon
415 observed in other NDDs[61]. Future work is needed to functionally validate these findings in our
416 model. Patch clamp, multi-electrode arrays, or calcium imaging will be important to quantify the
417 neural activity in these cells.
418

419 Our work in 3D DFBOs recapitulated many of our findings in 2D cultures, and in what is seen
420 clinically in affected individuals. When we measured the size of the DFBOs as they matured, we
421 found that they were initially larger, and then normalized in size compared to control (Fig. 5A).
422 At the time of last evaluation, the individual harboring the L48R variant in the BLBS cohort had
423 microcephaly[5]. Interestingly, the growth phenotype of individuals with BLBS seems to evolve
424 over time. The first reported individual with BLBS presented with macrocephaly and overgrowth
425 at birth but, at re-evaluation a decade later, exhibited microcephaly and severe
426 undergrowth[5,8,62]. D25 L48R DFBOs seem to capture the phenotypic transition observed in
427 affected individuals and could be used to study the mechanism driving this phenotype.
428
429 Another significant benefit of this DFBO model is that we can interrogate the impact of the L48R
430 variant on multiple cell types at once. Our SOX2 and PAX6 staining show that there is a
431 decrease in radial glia between D25 and D62 (Fig. 5B-C, Fig. S4C). The CTIP2 staining, which
432 shows an increase in intermediate progenitor neurons during this same window (Fig. S4D),
433 suggests that this decreased in radial glia is caused by a skewing towards the asymmetric
434 division of radial glia, away from the expected homeostatic balance between self-renewing
435 symmetric division and intermediate progenitor neuron-producing asymmetric division[57]. This is
436 further supported by the Ki67 and TUJ1 data, which show a decrease in proliferation
437 accompanied by an increase in neurons between D25 and D62 (Fig. B-D). Thus, L48R cells
438 ultimately differentiate into similar numbers of neurons at the cost of maintaining their progenitor
439 identity. However, the D62 L48R neurons either have delayed maturation (Fig. 6A), potentially
440 because of dysregulated TF occupancy, or may be dying due to grossly dysregulated gene
441 expression and chromatin occupancy. Taken together, these results indicate that L48R
442 progenitors are less able to proliferate and differentiate into mature neurons. While these data
443 suggest a depletion of radial glia, they do not address the question of whether radial glia-derived
444 cells skew towards a non-neuronal fate, as radial glia are the progenitors for both neurons and

445 certain glial subtypes (astrocytes) during neurodevelopment. The exhaustion of a replicative
446 pool which only exists for a transient period during neurodevelopment might also explain why
447 the central nervous system is universally affected but other organs are not.
448
449 We concluded our analyses at day 62 of maturation, which prevented us from interrogating glial
450 populations, which can only be analyzed in a DFBO model beginning at differentiation day 90[63].
451 Given that we found increases in glial markers in the 2D FBNs, understanding the effects on glia
452 in a 3D context will be informative, especially in understanding if these cells are skewed towards
453 a non-neuronal fate. The use of cerebral organoids, which are less guided than DFBOs, would
454 enable the study of additional cell types that make up hippocampal and retinal regions[64].
455 Oligodendrocyte-containing myelin organoids (myelinoids)[65] will also be important models to
456 understand the myelin-related anomalies observed in many individuals affected by BLBS.
457
458 Overall, our data suggest a model by which L48R acts through a gain-of-function mechanism
459 leading to increased *H3-3B* expression that results in the hyper-deposition of H3.3 into the
460 nucleosome which underlies changes in gene expression and chromatin accessibility.
461 Functionally, this causes dysregulation of cell adhesion, neurotransmission, and the balance
462 between excitatory and inhibitory signaling. The ability to define a proposed model with
463 modifiable mRNA and protein level readouts, as well as functional consequences, establishes
464 the necessary groundwork for future studies into therapeutic interventions. Specifically, our data
465 shows the upregulation of two $GABA_A$ receptor encoding genes, *GABRG3* and *GABRA5,* in
466 L48R NPCs. If GABA-mediated dysregulation is validated in future mechanistic work to underly
467 disease pathogenesis, this could be targeted through the repurposing of an FDA-approved class
468 of $GABA_A$ receptor selective positive allosteric modular antidepressants[66]. Further, because we
469 found that *H3-3B* itself is upregulated, suggesting a not previously defined gain-of-function
470 mechanism, targeting the mutated allele with an antisense oligonucleotide (ASO) or small

471 interfering RNA may be a viable therapeutic. Finally, if future work identifies the dysregulation of
472 hPTMs, perhaps an existing FDA-approved HDAC inhibitor could be repurposed for BLBS,
473 which is being explored for MDEMs[2]. Our results from one model have highlighted a few
474 therapeutic approaches, but intense future study into the mechanism of disease and the safety
475 of possible interventions is needed to understand what therapeutics would be most beneficial for
476 individuals affected by BLBS.
477
478 There are noteworthy strengths of our approach, which leverages 2D and 3D iPSC models
479 coupled with sequencing and IF, but we acknowledge the limitations of this work. First, these
480 studies were conducted in iPSCs that were derived from a single edited clone. To address this
481 limitation, we performed at least two separate differentiations of iPSCs to each cell type queried;
482 however, the gold standard would be to validate these findings in an independently generated
483 cell line. Further, it is not clear if all findings from our XX (female) model would be recapitulated
484 in an XY (male) model. Since there is an almost even number of males and females affected by
485 BLBS[8], these results would be strengthened if recapitulated in both an XX and XY model
486 system. It is also important to note that 70 unique variants are reported to cause BLBS[8], and we
487 investigated the effects of only a single BLBS-causing variant. Because of the phenotypic
488 variability observed in affected individuals and model systems[5,8,29], future studies in isogenic cell
489 lines from different origins harboring additional BLBS variants will be important in assessing the
490 generalizability of these findings to have the greatest impact for affected individuals.
491
492 In sum, we developed and interrogated a novel model of BLBS through the generation of an
493 isogenic L48R iPSC line differentiated to 2D NPCs, 2D FBNs, and 3D DFBOs. These data
494 support a model by which the L48R variant affects the proliferation and differentiation capacity
495 of NPCs in both 2D and 3D models. These early deficits prevent the maturation of neurons and
496 may skew cells away from a neuronal fate.

ACKNOWLEDGMENTS

We would like to sincerely thank the members of the BLBS community for sharing their information and journeys with us. Thank you also to Teodora Orendovici, PhD, Stephen Mahoney and Ashley Bushey from the CHOP High Throughput Sequencing Core for assistance with the ATAC-sequencing; Jean Ann Maguire, PhD from the CHOP iPSC core for generating the iPSC line; and Jonathan Billings, Kyra Booth, Tiancheng Wang and Kayleigh Ostberg from the CHOP Center for Applied Genomics for assistance with RNA-sequencing. Finally, we would like to acknowledge Elizabeth Gonzalez, Elizabeth Heller, PhD, Erica Korb, PhD, Ana Cristancho MD, PhD, and Colin Conine, PhD for their support throughout this manuscript's preparation.

CONTRIBUTIONS

Data Collection: RA, AKS, LMB, DLC, XMW

Data Analysis: AKS, RA, ELD

Figure Generation: AKS, RA, EEL

Conceived of study: RA, AKS, EJB

Drafted the manuscript: AKS, RA, EEL

Reviewed manuscript: EEL, ELD, DLC, XMW, KJC

FUNDING

Support for this work was provided by NICHD F30 1F30HD112125 (EEL); NIGMS T32 5T32GM008638 (ELD); NHGRI T32HG009495 and the Eagles Autism Foundation (DELC); the Chan-Zuckerberg Initiative Neurodegeneration Challenge Network, as well as the Burroughs Wellcome Fund and the Hartwell Foundation (EJKB).

522 **DATA AVAILABILITY**

523 The datasets generated during the current study will be available in the Gene Expression
524 Omnibus repository.

525 **COMPETING INTERESTS**

526 The authors declare no competing interests.

527

528 **METHODS**

529 **Maintenance, editing, and differentiation of 2D cells**

530 *iPSCs*

531 iPSCs were edited by the CHOP iPSC core as described[31]. The cells were single cell cloned
532 and frozen at an early passage. Edited and isogenic control iPSCs were maintained in
533 mTeSR™ Plus (STEMCELL Technologies 100-02 76) on 10cm plates coated with 1ug
534 Matrigel® hESC-Qualified Matrix (Corning 354277) and collected at passage 30 for RNA-
535 sequencing.

536 *NPCs*

537 Cells were differentiated to NPCs using STEMdiff™ SMADi Neural Induction Kit following the
538 monolayer culture protocol (STEMCELL Technologies 08582). Briefly, for each well, 2 million
539 iPSCs were resuspended in STEMdiff™ Neural Induction Medium + SMADi + 10 μM Y-27632
540 and plated in each well of a 6-well plate coated with 1ug of Matrigel. Cells well given a full
541 medium change with STEMdiff™ Neural Induction Medium + SMADi except on days when they
542 were passaged (approximately every seven days). Cells were collected at passage four for
543 RNA-sequencing. At the end of differentiation, cells were cryopreserved in STEMdiff™ Neural
544 Progenitor Freezing Medium.

545 *FBNs*

546 NPCs were thawed and differentiated to forebrain neurons using STEMdiff™ Forebrain Neuron
547 Differentiation Kit (STEMCELL Technologies 08600). Briefly, NPCs were plated in PLO-Laminin
548 coated 6 well plates (1.25 million cells per well) in STEMdiff™ Neural Induction Medium +
549 SMADi, and after 24 hours, media was changed to STEMdiff™ Forebrain Neuron Differentiation
550 medium. Cells were cultured in the same medium until they reached 80-90% confluency and
551 passaged on to 12 well plates coated with PLO-laminin at a density of 175,000 cells per well in
552 STEMdiff™ Forebrain Neuron Maturation medium. The FBNs were matured up to three weeks.

553

554 **RNA sequencing**

555 *RNA extraction, library prep & sequencing*

556 Total RNA was extracted from iPSCs and NPCs using the Zymo Direct-zol RNA Miniprep (Cat #
557 R2050 or from FBNs with the Zymo Direct-zol RNA Microprep (Cat # R2062). QC was
558 performed using the Gx Bioanalyzer/Agilent Tapestation for traces and Qubit for concentration.
559 Libraries were prepared using the Illumina Stranded Total RNA Prep, Ligation with Ribo-Zero
560 Plus. 200ng of cDNA libraries were amplified using 12 cycles of PCR and sequenced on a
561 v1.5_SP (200 cycle) flow cell with the NovaSeq6000. Reads were demultiplexed using Dragen
562 Demultiplexing.

563

564 *Data analysis*

565 Reads were aligned to Homo_sapiens.GRCh38.cdna.all using kallisto[32](v0.50.1). Differential
566 expression was calculated using DeSeq2[33](v1.44.0) in R v 4.4.0 using RStudio 2024.04.1+748.
567 Volcano plots were made using EnhancedVolcano[34](v1.22.0). We defined genes with
568 significantly altered expression with an adjusted p-value ≤ 0.05 and log fold change with an
569 absolute value of ≥ 1. GO analyses were performed using clusterProfiler[35] (v4.12.0) using
570 biological pathway terms. Revigo[36] was used to summarize GO terms and these terms were

571 clustered using a distance matrix and hierarchical clustering. Each cluster was labeled with one
572 representative term, obtained by selecting the term within each cluster with the largest LogSize,
573 the Log10 value of the number of annotations for GO Term ID in selected species in the
574 European Bioinformatics Institute Gene Ontology Annotation database. The list of astrocyte
575 specific genes used to analyze the FBN data was obtained from PanglaoDB[37] and filtered for
576 human and a specificity score ≤ 0.5 (meaning that these genes are expressed in cells other than
577 astrocytes less than or equal to 50% of the time).
578
579 **Western Blots**
580 Histones were extracted using the Abcam Histone Extraction Kit (ab113476). Protein
581 concentration was quantified using the Pierce™ BCA Protein Assay Kit (A65453) and run using
582 the SkanIt software v6.1 by measuring the absorbance at 550nm. 2ug of histone extract was
583 loaded/Western. Subcellular fractionation was performed using Subcellular Protein Fractionation
584 Kit for Cultured Cells (Thermo # 78840) and protein quantification was performed as described
585 above. 21ug of cytoplasmic fraction or 3ug of chromatin fraction were separated by
586 electrophoresis using NuPAGE™ 4-12% Bis-Tris Protein Gel (ThermoFisher Scientific). Proteins
587 were transferred to a polyvinylidene difluoride (PVDF) membrane using an XCell SureLock Mini-
588 Cell Electrophoresis System (ThermoFisher Scientific). The membrane was blocked using 5%
589 dry milk in Tris-Buffered Saline (Bio Basic, Markham) with Tween-20 for 1 hour at room
590 temperature. After briefly rinsing with Tris-Buffered Saline (Bio Basic, Markham) with Tween-20,
591 the membrane was incubated overnight at 4°C with primary antibody (Table 5). The membrane
592 was then washed with Tris-Buffered Saline with Tween-20 and incubated in secondary antibody
593 diluted 1:10,000 (Goat Anti-Rabbit IgG Polyclonal from LI-COR Biosciences) for 1 hour at room
594 temperature. Blots were visualized using the ODYSSEY® DLx (LI-COR Biosciences) and
595 quantified using ImageJ.
596

597 **ATAC-sequencing**:

598 *Library preparation & sequencing*

599 ATAC-seq libraries were generated using the ATAC-seq Kit from Diagenode (Diagenode, A
600 Hologic Company) according to manufacturer instructions. Briefly, cells were centrifuged at 500
601 × g for 10 minutes using a fixed angle refrigerated centrifuge, followed by a wash with 500 µl of
602 cold 1x PBS and a second centrifugation at 500 × g for 10 minutes. Cells were counted and
603 approximately 50,000 cells were lysed using cold ATAC lysis + Digitonin (2%). Immediately after
604 lysis, cell nuclei were spun again at 500 × g for 10 minutes and separated from the lysis buffer.
605 Immediately following the nuclei extraction, the pellet was resuspended in transposase reaction
606 mix. The transposition reaction was carried out for 30 minutes at 37 °C. Directly following
607 transposition the samples were purified using the kit's provided columns. Following purification,
608 library fragments were amplified using 1x Amplification master mix and the following PCR
609 conditions: 72°C for 5 minutes, 98°C for 30 seconds, followed by thermocycling at 98°C for 10
610 seconds, 63°C for 30 seconds and 72°C for 1 minute for 5 cycles, in this step Unique Dual
611 Indexes Primer Pair were incorporated for multiplexed sequencing. To reduce amplification bias
612 after the first 5 cycles, qPCR was used to determine the number of PCR cycles needed to
613 produce the concentration required for sequencing. Each pre-amplified library was further
614 amplified for 6 cycles as determined by the qPCR step. Final libraries were bead purified
615 (Beckman Coulter), then assessed for size distribution and concentration using the Bioanalyzer
616 High Sensitivity DNA Kit (Agilent Technologies). The resulting libraries were pooled in equal
617 molarity, the pool was diluted to approximately 2 nM using 10 mM Tris-HCl, pH 8.5, denatured,
618 and loaded onto a P1-100 (2x50) flow cell on an Illumina NextSeq 6000 (Illumina, Inc.)
619 according to the manufacturer's instructions. De-multiplexed and adapter-trimmed sequencing
620 reads were generated using bcl2fastq.

621

622 *Data processing and analysis*

623 Reads were aligned to *Homo* sapiens genome build Genome Reference Consortium Human
624 Build 38 (GRCh38) with botwie2[38] (v2.5.4). PCR duplicates were removed using picard[39]
625 (v3.2.0), mitochondrial regions were removed, and blacklisted regions were identified using
626 ENCODE (GRCh38_unified_blacklist.bed) and removed. Peaks were called using macs3[40]
627 (v3.0.1) with a q-value cutoff of 0.05. Peaks were annotated using ChIPSeeker[36](v1.40.0).
628 DiffBind[69](v3.14.0) was used to determine differential accessibility between L48R and control
629 peaks and plotted using DiffBind profile plot. For transcription factor footprinting, reads were
630 shifted to account for the Tn5 overhang using ATACshift from deeptools[44], and motifs were
631 identified using ATACseqTFEA[55] with human motifs "best_curated_Human.rds". Genome
632 browser plots were made using IGV(v2.17.4)
633
634 **qPCR validation**:
635 Total RNA was extracted from iPSC and NPCs using the Zymo Direct-zol RNA Miniprep (Cat #
636 R2050 or from FBNs with the Zymo Direct-zol RNA Microprep (Cat # R2062). The concentration
637 was quantified using the NanoDrop 8000 UV-Vis Spectrophotometer (Thermo Scientific). cDNA
638 was synthesized from 1ug of RNA using Superscript IV (Thermo Scientific). RT-qPCR reactions
639 were set up using cDNA, 2X PowerUp™ SYBR® Green Master Mix (Applied Biosystems), gene
640 specific primers using GAPDH as an internal control. Samples were run in a 96-well plate on the
641 QuantStudio™ 3 System using the Comparative C_T ($\Delta\Delta C_T$) method. The primers used are listed
642 in Table 6.
643
644 **Dorsal Forebrain Organoids (DFBOs)**
645 Forebrain organoids were generated using STEMdiff™ Dorsal Forebrain Organoid
646 Differentiation Kit (Cat: 08620) according to manufacturer instructions, and this protocol was
647 adopted from[45]. Briefly, embryoid bodies (EB) were generated in AggreWell™800 24-well plate
648 in a seeding medium with 10,000 cells per microwell. This method will generate 500 equalized

649 EBs per one well of a 24-well plate. After 24 hours, the media was changed to a Forebrain
650 Organoid formation medium, and the EB was maintained for five days. EBs were transferred to
651 ultra-low attachment 6-well plates (40 organoids per well) in organoid expansion medium.
652 Organoids were maintained in the same medium for a period of 25 days with frequent media
653 changes. After the neuroectoderm expansion, the media was changed to the Forebrain
654 Organoid Differentiation medium and maintained organoids until day 43 with frequent media
655 changes. For long-term maintenance of DFBO, the media was changed to a Forebrain Organoid
656 maintenance medium. For the analysis, we harvested organoids at day 25 (Neuroectoderm
657 expansion) and day 62 (DFBO maturation).
658
659 *Embedding*
660 Organoids were washed with D-PBS then fixed in 5mL fresh 4% paraformaldehyde (PFA)
661 solution and incubated overnight at 4°C. Organoids were washed in PBS-T and stored in PBS-T
662 at 4°C for 1 week. Organoids were then incubated in 30% sucrose solution and equilibrated
663 overnight at 4°C. Equilibration was complete once organoids were no longer floating in the 30%
664 sucrose solution. Organoids were then incubated at 37°C in porcine gelatin for 1 hour and
665 embedded in this solution in embedding molds. Six organoids were embedded per block and
666 allowed to solidify at RT and 4°C before being snap frozen in a dry ice/ethanol slurry (dry ice +
667 100% ethanol). Frozen samples were stored at -80°C until ready for cryosectioning.
668
669 *Cryosectioning and Immunoflourescence Staining*:
670 Blocks were removed from the -80°C freezer and allowed to equilibrate to -26°C in the cryostat
671 (Microm HM 505E, CHOP Pathology Core) for at least 30 minutes before sectioning. Sections
672 were cut at 16um using a high-profile blade (Leica Biosystems 14035838926) and mounted on
673 colorfrost Plus Microscope Slides (Fisher Scientific 12-550-17). Slides were stored at -80C until
674 staining. Slides were allowed to come to room temperature before staining. Hydrophobic

675 barriers were drawn around sections. Antigen retrieval using sodium citrate pH 6.0, was
676 performed for the CTIP2 staining. Slides were steamed in a food steamer for 20 minutes in
677 citrate buffer, washed with PBS-T at 37°C for 10 minutes to fully remove gelatin from slides,
678 blocked in a humidified chamber for 1 hour, and incubated with primary antibody overnight. The
679 next day, primary antibody solutions were removed, slides were washed 3 times with PBS-T
680 and incubated in secondary antibody at room temperature in a humified chamber for 2 hours.
681 After incubation, secondary antibody solution was removed, slides were washed 3 times with
682 PBS-T for 30 minutes, allowed to air dry for 5 minutes, then one drop of PermaFluor™ was
683 added to slides to add coverslip.
684
685 *Image acquisition and quantification*
686 Images for quantification were acquired using a Keyence BZ-X800 (Itasca, IL) or the Leica
687 STELLARIS 5 Confocal Microscope. 10x images taken of DFBOs were stitched together using
688 Keyence BZ-X Series Analysis Software. FIJI (v 2.14.0/1.54f) was used to quantify the fraction
689 of cells that were positive for cell fate markers. Images were separated by channel, converted to
690 binary, then particles were analyzed for each image. Corrected fluorescence was calculated by
691 dividing the total fluorescence of each image by the total fluorescence intensity of its respective
692 DAPI stain.
693
694 **Statistics**
695 Comparisons were made between Control and L48R cells. For RT-qPCR and IF, statistics were
696 calculated using Welch Two Sample t-test in R v 4.4.0 using RStudio 2024.04.1+748. A p-value
697 ≤ 0.05 is denoted with *, p-value ≤ 0.01 is denoted with **, and p-value ≤ 0.001 is denoted with
698 ***. For RNA-seq, statistics were calculated using DESeq2[33], and for ATAC-seq statistics were
699 calculated using DiffBind[43].

700

701

702 **Figure Legends:**

703 **Figure 1. Generation and initial characterization of L48R 2D iPSCs, NPCs and FBNs.** A)
704 c.146T>G *H3-3B* Leu48Arg (L48R) variant was introduced to CHOPWT14 hiPSCs using
705 CRISPR HDR. The heterozygous L48R edited cells were single cell cloned to generate a pure
706 population of edited cells. Both L48R and isogenic control cells were differentiated into NPCs
707 (STEMdiff™ SMADi Neural Induction Kit) and FBNs (Stem Cell Technologies STEMDiff
708 Forebrain Neuronal Differentiation Kit). B) RT-qPCR for pluripotency markers in iPSCs and
709 NPCs. *OCT4* p-value = 0.09808 in iPSCs, p-value = 0.2372 in NPCs; *NANOG* p-value = *0.143*
710 in iPSCs, p-value = 0.00836 in NPCs. C) RT-qPCR gene expression analysis of NPC markers.
711 *SOX2* iPSC p-value = 0.954, p-value = 0.02608 in NPCs. *NESTIN* p-value = 0.1357 in iPSCs, p-
712 value = 0.09037 in NPCs. D) Immunofluorescence of FBNs stained with DAPI, MAP2 (neuronal
713 extensions), VGLUT1 (glutamatergic neurons). E) Quantification of images in D) using FIJI. n =
714 10 images from 3 replicates for each condition. MAP2 p-value = 9.536e-05, VGLUT1 p-value =
715 6.694e-05. F) RT-qPCR for astrocyte marker *GFAP*. p-value = 1.104e-06.

716

717 **Figure 2. Transcriptomic changes in L48R progenitor cells affect differentiation into**
718 **FBNs.** A) Volcano plot of L48R vs control iPSCs and B) NPCs. Blue dots represent
719 downregulated genes, red = upregulated genes. Dotted horizontal line denotes an adjusted p-
720 value of ≤ 0.01 and dotted vertical lines indicate a log2fold change (LFC) with an absolute value
721 of ≥ 1. C) GO analysis for biological function of all significantly differentially expressed genes
722 between L48R and control NPCs. D) Heatmap representing the Z-scored LFCs of the genes
723 comprising cell adhesion and axonogenesis GO terms. Descriptions of function and disease
724 association are in Table 1 for these genes. E) Volcano plot of L48R vs control FBNs. Blue dots

725 represent downregulated genes, red = upregulated genes. Dotted horizontal line denotes an
726 adjusted p-value of ≤ 0.01 and dotted vertical lines indicate a LFC with an absolute value of ≥ 1.
727 F) Upset plot of shared hits between the RNA-seq datasets generated in iPSCs, NPCs and
728 FBNs. n = 2 commonly downregulated genes, n=10 commonly upregulated genes.
729 **Figure 3. L48R variant alters chromatin accessibility and the occupancy of transcription**
730 **factors important for neuronal development.** A) Pie plot of the genomic annotations of sites
731 that are differentially accessible in L48R vs control NPCs (identified using DiffBind). B) Genomic
732 heatmap of differentially accessible sites grouped by sites that are more accessible in L48R
733 (top, green), and those that are less accessible in L48R NPCs (bottom, purple). C) GO
734 enrichment of regions with increased chromatin accessibility, annotated by nearest gene, in
735 L48R NPCs compared to control. D) RNA-seq (top, blue) and ATAC-seq (bottom, pink) tracks
736 for *PLXNA3*, an axonal gene with increased accessibility and expression in L48R compared to
737 control NPCs. E) Volcano plot of transcription factors with increased occupancy (red dots) or
738 decreased occupancy (blue dots) in L48R NPCs vs control. F) REVIGO summary of GO terms
739 associated with transcription factors in E) clustered by similarity.
740
741 **Figure 4. Chromatin accessibility changes in L48R 2D NPCs affect expression of genes**
742 **important for cell adhesion and neurotransmission.** A) Venn diagram of overlap of
743 significantly downregulated genes in RNA- and ATAC-seq. Six commonly downregulated genes
744 are listed. B) RNA-seq (top, blue) and ATAC-seq (bottom, pink) tracks for representative gene
745 *CDH4*. C) RT-qPCR validation of *CDH4* mRNA levels at different time points in differentiation
746 from iPSC, NPC, to FBN. ΔΔ Ct values are normalized to *GAPDH*. IPSC p-value = 9.834e-05,
747 NPC p-value = 0.0008733, FBN p-value = 0.001522. D) Venn diagram of overlap of significantly
748 upregulated genes in both datasets. 22 commonly upregulated genes are listed. E-F) RNA- and
749 ATAC-seq tracks + RT-qPCR validation of *GABRG3*. IPSC p-value = 0.002509, NPC p-value =

750 0.008845, FBN p-value = 0.02047. (G-H) RNA- and ATAC-seq tracks + RT-qPCR validation of
751 *DPP6.* iPSC p-value = 0.0001059, NPC p-value = 2.596e-05, FBN p-value = 0.005359.
752
753 **Figure 5. L48R variant perturbs progenitor populations in 3D DFBOs.** A) Left:
754 Representative images of organoids at D25, 45, and 62. Scale bar = 500um. D25 images were
755 taken at 10X magnification, D45 and D62 images were taken at 4x magnification, scale bar =
756 500µm Right: Quantification of organoid size using Qupath[67]. n = 6 control D25, n = 7 L48R
757 D25; n = 6 control and L48R D45; n = 15 control D60, n = 16 L48R D62. D25 p-value = 0.01684,
758 D48 p-value = 0.7073, D62 p-value = 0.2947. B) Organoids collected at D25 (left) and D62
759 (right) stained with neuronal marker TUJ1 (green), progenitor marker SOX2 (pink) and DAPI
760 (blue). Top = 10x magnification, bottom = 20X magnification. C) Quantification of 10x images in
761 B at D25 (left) and D62 (right). n = 6 organoids (D25), n = 4 organoids (D62). Each dot
762 represents 1 image. TUJ1 D25 p-value = 0.002887, D62 p-value = 0.5016. SOX1 D25 p-value =
763 0.3507, D62 p-value = 0.005652. D) Organoids stained for SOX2 (green) and proliferative
764 marker Ki67 (red) at both day 25 (left) and day 62 (right). The same images are shown in color
765 with all three markers and black and white with only Ki67.
766
767 **Figure 6. L48R DFBOs have fewer mature neurons and increased GABA abundance.** A)
768 D62 DFBOs stained with MAP2 (green) and PAX6 (red). Two representative images taken at
769 10X are displayed along with one representative image taken at 20X magnification. Right:
770 Images taken at both magnifications were quantified. Corrected total fluorescence was
771 calculated by dividing the fluorescence intensity of MAP2 by the fluorescence intensity of DAPI
772 for each image. p-value = 0.006039. B) 10X images of D62 DFBOs stained with GABA (red)
773 and NeuN (green). Images were quantified as described in (A). p-value = 0.03561. C) RT-qPCR
774 quantification of *GABRG3* levels in n = 4 DFBOs for both genotypes. p-value = 3.597e-05.
775

776 **Supplementary Figures:**

777 **Supplementary Figure 1 Characterization of 2D L48R iPSCs, NPCs and FBNs.** A) Sanger
778 sequencing verification of isogenic control (top) and heterozygous c.146T>C edit in CHOPWT14
779 cells (bottom). B) Description of CHOPWT14 iPSCs. Method = reprogramming method. C) IF
780 analysis in FBNs of TUJ1 (neurons) and GFAP (glia) collected at day 20. D) Quantification of n
781 = 5 z-stacks for control, and n = 6 z-stacks for L48R FBNs. Corrected total fluorescence was
782 calculated by dividing the fluorescence intensity of TUJ1 and GFAP by the fluorescence
783 intensity of DAPI for each image. TUJ1 p-value = 0.06939, GFAP p-value = 0.159. E) RT-qPCR
784 analysis of *MAP2* mRNA levels in iPSCs and FBNs. p-value = 0.4915 in iPSCs, p-value =
785 0.2222 in FBNs.

786

787 **Supplementary Figure 2 Transcriptomic dysregulation induced by L48R variant** A) PCA of
788 L48R and control iPSCs, NPCs and FBNS, colored by genotype. B) REVIGO summary of GO
789 terms associated with significantly upregulated genes in FBNs, clustered by similarity. C)
790 Heatmap of z-scored LFCs of astrocyte genes (from [37]). D) BrdU labeling of control and L48R
791 FBNs. E) GO plot of top 15 pathways downregulated in L48R FBNs compared to control FBNs.
792 F) GO plot of significantly dysregulated genes in both L48R NPCs and FBNs compared to
793 control.

794

795 **Supplementary Figure 3 H3.3 deposition is altered in L48R cells, resulting in changes in**
796 **chromatin landscape.** A) log2normalized counts of *H3-3B* and *H3-3B* from the NPC RNA-seq.
797 B) RT-qPCR analysis of *H3-3B* in iPSCs (p-value = 0.3348), NPCs (p-value = 0.04321), and
798 FBNs (p-value = 0.0006555). B) Western blot on nuclear extracted H3.3 and H4 as a loading
799 control. C) Western blot probing for H3.3 in cytoplasmic and chromatin-bound fractions. D) IF for
800 H3.3 and MAP2 in Control and L48R FBNs (left). Quantification of H3.3 fluorescence (right). p-
801 value < 2.2e-16. E) RNA- and ATAC-seq tracks for *RBFOX1*. F) log2-normalized counts for

802 additional genes that were affected in both ATAC- and RNA-seq. Genes to the left of the
803 dashed line were down and those to the right were upregulated.
804
805 **Supplementary Figure 4 Cell identity analysis in 3D DFBOs corroborates 2D findings.** A)
806 Schematic of the dorsal forebrain organoid protocol employed in this study. Organoids were
807 collected for sectioning at D25, and for RT-qPCR analysis and sectioning at D62. B) Images
808 taken at 4X magnification of control (top) and L48R (bottom) organoids at D62 showing
809 differences in NE buds (denoted by errors). C) IF for PAX6 (red) at D62 (top) and quantification
810 of corrected fluorescence intensity n = 6 organoids, control and n = 4 organoids, L48R (bottom).
811 p-value = 0.3291 D) CTIP2 staining at D25 and D62, along with corrected total fluorescence
812 quantifications of n = 6 organoids (control) or n = 4 organoids (L48R). D25 p-value = 0.1045,
813 D62 p-value = 0.138.
814
815
816 **REFERENCES**

817 1. Ropers, H.H. (2010). Genetics of early onset cognitive impairment. Annu. Rev.
818 Genomics Hum. Genet. *11*, 161–187. https://doi.org/10.1146/annurev-genom-
819 082509-141640.

820 2. Harris, J.R., Gao, C.W., Britton, J.F., Applegate, C.D., Bjornsson, H.T., and Fahrner,
821 J.A. (2024). Five years of experience in the Epigenetics and Chromatin Clinic: what
822 have we learned and where do we go from here? Hum. Genet. *143*, 607–624.
823 https://doi.org/10.1007/s00439-023-02537-1.

824 3. Tessadori, F., Giltay, J.C., Hurst, J.A., Massink, M.P., Duran, K., Vos, H.R., van Es,
825 R.M., Deciphering Developmental Disorders Study, Scott, R.H., van Gassen, K.L.I.,
826 et al. (2017). Germline mutations affecting the histone H4 core cause a
827 developmental syndrome by altering DNA damage response and cell cycle control.
828 Nat. Genet. *49*, 1642–1646. https://doi.org/10.1038/ng.3956.

829 4. Tessadori, F., Duran, K., Knapp, K., Fellner, M., Deciphering Developmental
830 Disorders Study, Smithson, S., Beleza Meireles, A., Elting, M.W., Waisfisz, Q.,
831 O'Donnell-Luria, A., et al. (2022). Recurrent de novo missense variants across

832 multiple histone H4 genes underlie a neurodevelopmental syndrome. Am. J. Hum.
833 Genet. *109*, 750–758. https://doi.org/10.1016/j.ajhg.2022.02.003.

834 5. Bryant, L., Li, D., Cox, S.G., Marchione, D., Joiner, E.F., Wilson, K., Janssen, K.,
835 Lee, P., March, M.E., Nair, D., et al. (2020). Histone H3.3 beyond cancer: Germline
836 mutations in Histone 3 Family 3A and 3B cause a previously unidentified
837 neurodegenerative disorder in 46 patients. Sci. Adv. *6*, eabc9207.
838 https://doi.org/10.1126/sciadv.abc9207.

839 6. Maver, A., Čuturilo, G., Ruml, S.J., and Peterlin, B. (2019). Clinical Next Generation
840 Sequencing Reveals an H3F3A Gene as a New Potential Gene Candidate for
841 Microcephaly Associated with Severe Developmental Delay, Intellectual Disability
842 and Growth Retardation. Balk. J. Med. Genet. BJMG *22*, 65–68.
843 https://doi.org/10.2478/bjmg-2019-0028.

844 7. Okur, V., Chen, Z., Vossaert, L., Peacock, S., Rosenfeld, J., Zhao, L., Du, H.,
845 Calamaro, E., Gerard, A., Zhao, S., et al. (2021). De novo variants in H3-3A and H3-
846 3B are associated with neurodevelopmental delay, dysmorphic features, and
847 structural brain abnormalities. NPJ Genomic Med. *6*, 104.
848 https://doi.org/10.1038/s41525-021-00268-8.

849 8. Layo-Carris, D.E., Lubin, E.E., Sangree, A.K., Clark, K.J., Durham, E.L., Gonzalez,
850 E.M., Smith, S., Angireddy, R., Wang, X.M., Weiss, E., et al. (2024). Expanded
851 phenotypic spectrum of neurodevelopmental and neurodegenerative disorder
852 Bryant-Li-Bhoj syndrome with 38 additional individuals. Eur. J. Hum. Genet.
853 https://doi.org/10.1038/s41431-024-01610-1.

854 9. Alves, C. a. P.F., Sherbini, O., D'Arco, F., Steel, D., Kurian, M.A., Radio, F.C.,
855 Ferrero, G.B., Carli, D., Tartaglia, M., Balci, T.B., et al. (2022). Brain Abnormalities in
856 Patients with Germline Variants in H3F3: Novel Imaging Findings and Neurologic
857 Symptoms Beyond Somatic Variants and Brain Tumors. AJNR Am. J. Neuroradiol.
858 *43*, 1048–1053. https://doi.org/10.3174/ajnr.A7555.

859 10. Funk, O.H., Qalieh, Y., Doyle, D.Z., Lam, M.M., and Kwan, K.Y. (2022). Postmitotic
860 accumulation of histone variant H3.3 in new cortical neurons establishes neuronal
861 chromatin, transcriptome, and identity. Proc. Natl. Acad. Sci. U. S. A. *119*,
862 e2116956119. https://doi.org/10.1073/pnas.2116956119.

863 11. Jin, C., Zang, C., Wei, G., Cui, K., Peng, W., Zhao, K., and Felsenfeld, G. (2009).
864 H3.3/H2A.Z double variant-containing nucleosomes mark "nucleosome-free regions"
865 of active promoters and other regulatory regions. Nat. Genet. *41*, 941–945.
866 https://doi.org/10.1038/ng.409.

867 12. Goldberg, A.D., Banaszynski, L.A., Noh, K.-M., Lewis, P.W., Elsaesser, S.J., Stadler,
868 S., Dewell, S., Law, M., Guo, X., Li, X., et al. (2010). Distinct factors control histone
869 variant H3.3 localization at specific genomic regions. Cell *140*, 678–691.
870 https://doi.org/10.1016/j.cell.2010.01.003.

13. Chen, P., Zhao, J., Wang, Y., Wang, M., Long, H., Liang, D., Huang, L., Wen, Z., Li, W., Li, X., et al. (2013). H3.3 actively marks enhancers and primes gene transcription via opening higher-ordered chromatin. Genes Dev. *27*, 2109–2124. https://doi.org/10.1101/gad.222174.113.

14. Jin, C., and Felsenfeld, G. (2007). Nucleosome stability mediated by histone variants H3.3 and H2A.Z. Genes Dev. *21*, 1519–1529. https://doi.org/10.1101/gad.1547707.

15. Chow, C.-M., Georgiou, A., Szutorisz, H., Maia e Silva, A., Pombo, A., Barahona, I., Dargelos, E., Canzonetta, C., and Dillon, N. (2005). Variant histone H3.3 marks promoters of transcriptionally active genes during mammalian cell division. EMBO Rep. *6*, 354–360. https://doi.org/10.1038/sj.embor.7400366.

16. Jin, C., and Felsenfeld, G. (2006). Distribution of histone H3.3 in hematopoietic cell lineages. Proc. Natl. Acad. Sci. U. S. A. *103*, 574–579. https://doi.org/10.1073/pnas.0509974103.

17. Deaton, A.M., Gómez-Rodríguez, M., Mieczkowski, J., Tolstorukov, M.Y., Kundu, S., Sadreyev, R.I., Jansen, L.E., and Kingston, R.E. (2016). Enhancer regions show high histone H3.3 turnover that changes during differentiation. eLife *5*, e15316. https://doi.org/10.7554/eLife.15316.

18. Kraushaar, D.C., Jin, W., Maunakea, A., Abraham, B., Ha, M., and Zhao, K. (2013). Genome-wide incorporation dynamics reveal distinct categories of turnover for the histone variant H3.3. Genome Biol. *14*, R121. https://doi.org/10.1186/gb-2013-14-10-r121.

19. Herre, M., and Korb, E. (2019). The chromatin landscape of neuronal plasticity. Curr. Opin. Neurobiol. *59*, 79–86. https://doi.org/10.1016/j.conb.2019.04.006.

20. Maze, I., Wenderski, W., Noh, K.-M., Bagot, R.C., Tzavaras, N., Purushothaman, I., Elsässer, S.J., Guo, Y., Ionete, C., Hurd, Y.L., et al. (2015). Critical Role of Histone Turnover in Neuronal Transcription and Plasticity. Neuron *87*, 77–94. https://doi.org/10.1016/j.neuron.2015.06.014.

21. Piña, B., and Suau, P. (1987). Changes in histones H2A and H3 variant composition in differentiating and mature rat brain cortical neurons. Dev. Biol. *123*, 51–58. https://doi.org/10.1016/0012-1606(87)90426-x.

22. Lan, F., and Shi, Y. (2015). Histone H3.3 and cancer: A potential reader connection. Proc. Natl. Acad. Sci. U. S. A. *112*, 6814–6819. https://doi.org/10.1073/pnas.1418996111.

23. Kallappagoudar, S., Yadav, R.K., Lowe, B.R., and Partridge, J.F. (2015). Histone H3 mutations--a special role for H3.3 in tumorigenesis? Chromosoma *124*, 177–189. https://doi.org/10.1007/s00412-015-0510-4.

24. Deshmukh, S., Ptack, A., Krug, B., and Jabado, N. (2022). Oncohistones: a roadmap to stalled development. FEBS J. *289*, 1315–1328. https://doi.org/10.1111/febs.15963.

25. Schwartzentruber, J., Korshunov, A., Liu, X.-Y., Jones, D.T.W., Pfaff, E., Jacob, K., Sturm, D., Fontebasso, A.M., Quang, D.-A.K., Tönjes, M., et al. (2012). Driver mutations in histone H3.3 and chromatin remodelling genes in paediatric glioblastoma. Nature *482*, 226–231. https://doi.org/10.1038/nature10833.

26. Khuong-Quang, D.-A., Buczkowicz, P., Rakopoulos, P., Liu, X.-Y., Fontebasso, A.M., Bouffet, E., Bartels, U., Albrecht, S., Schwartzentruber, J., Letourneau, L., et al. (2012). K27M mutation in histone H3.3 defines clinically and biologically distinct subgroups of pediatric diffuse intrinsic pontine gliomas. Acta Neuropathol. (Berl.) *124*, 439–447. https://doi.org/10.1007/s00401-012-0998-0.

27. Wu, G., Broniscer, A., McEachron, T.A., Lu, C., Paugh, B.S., Becksfort, J., Qu, C., Ding, L., Huether, R., Parker, M., et al. (2012). Somatic histone H3 alterations in pediatric diffuse intrinsic pontine gliomas and non-brainstem glioblastomas. Nat. Genet. *44*, 251–253. https://doi.org/10.1038/ng.1102.

28. Behjati, S., Tarpey, P.S., Presneau, N., Scheipl, S., Pillay, N., Van Loo, P., Wedge, D.C., Cooke, S.L., Gundem, G., Davies, H., et al. (2013). Distinct H3F3A and H3F3B driver mutations define chondroblastoma and giant cell tumor of bone. Nat. Genet. *45*, 1479–1482. https://doi.org/10.1038/ng.2814.

29. Khazaei, S., Chen, C.C.L., Andrade, A.F., Kabir, N., Azarafshar, P., Morcos, S.M., França, J.A., Lopes, M., Lund, P.J., Danieau, G., et al. (2023). Single substitution in H3.3G34 alters DNMT3A recruitment to cause progressive neurodegeneration. Cell *186*, 1162-1178.e20. https://doi.org/10.1016/j.cell.2023.02.023.

30. Yang, Q., Hong, Y., Zhao, T., Song, H., and Ming, G.-L. (2022). What Makes Organoids Good Models of Human Neurogenesis? Front. Neurosci. *16*, 872794. https://doi.org/10.3389/fnins.2022.872794.

31. Maguire, J.A., Cardenas-Diaz, F.L., Gadue, P., and French, D.L. (2019). Highly Efficient CRISPR-Cas9-Mediated Genome Editing in Human Pluripotent Stem Cells. Curr. Protoc. Stem Cell Biol. *48*, e64. https://doi.org/10.1002/cpsc.64.

32. Bray, N.L., Pimentel, H., Melsted, P., and Pachter, L. (2016). Near-optimal probabilistic RNA-seq quantification. Nat. Biotechnol. *34*, 525–527. https://doi.org/10.1038/nbt.3519.

33. Love, M.I., Huber, W., and Anders, S. (2014). Moderated estimation of fold change and dispersion for RNA-seq data with DESeq2. Genome Biol. *15*, 550. https://doi.org/10.1186/s13059-014-0550-8.

34. Blighe, Kevin, Nitesh, Turaga, Grionia, Andrea, Turkes, Emir, and Benjamin, Ostendorf (2018). EnhancedVolcano: Publication-ready volcano plots with enhanced colouring and labeling.

35. Yu, G., Wang, L.-G., Han, Y., and He, Q.-Y. (2012). clusterProfiler: an R package for comparing biological themes among gene clusters. Omics J. Integr. Biol. *16*, 284–287. https://doi.org/10.1089/omi.2011.0118.

36. Supek, F., Bošnjak, M., Škunca, N., and Šmuc, T. (2011). REVIGO summarizes and visualizes long lists of gene ontology terms. PloS One *6*, e21800. https://doi.org/10.1371/journal.pone.0021800.

37. Franzén, O., Gan, L.-M., and Björkegren, J.L.M. (2019). PanglaoDB: a web server for exploration of mouse and human single-cell RNA sequencing data. Database J. Biol. Databases Curation *2019*, baz046. https://doi.org/10.1093/database/baz046.

38. Langmead, B., and Salzberg, S.L. (2012). Fast gapped-read alignment with Bowtie 2. Nat. Methods *9*, 357–359. https://doi.org/10.1038/nmeth.1923.

39. Broad Institute Picard Toolkit.

40. Zhang, Y., Liu, T., Meyer, C.A., Eeckhoute, J., Johnson, D.S., Bernstein, B.E., Nusbaum, C., Myers, R.M., Brown, M., Li, W., et al. (2008). Model-based analysis of ChIP-Seq (MACS). Genome Biol. *9*, R137. https://doi.org/10.1186/gb-2008-9-9-r137.

41. Yu, G., Wang, L.-G., and He, Q.-Y. (2015). ChIPseeker: an R/Bioconductor package for ChIP peak annotation, comparison and visualization. Bioinformatics *31*, 2382–2383. https://doi.org/10.1093/bioinformatics/btv145.

42. Wang, Q., Li, M., Wu, T., Zhan, L., Li, L., Chen, M., Xie, W., Xie, Z., Hu, E., Xu, S., et al. (2022). Exploring Epigenomic Datasets by ChIPseeker. Curr. Protoc. *2*, e585. https://doi.org/10.1002/cpz1.585.

43. Ross-Innes, C.S., Stark, R., Teschendorff, A.E., Holmes, K.A., Ali, H.R., Dunning, M.J., Brown, G.D., Gojis, O., Ellis, I.O., Green, A.R., et al. (2012). Differential oestrogen receptor binding is associated with clinical outcome in breast cancer. Nature *481*, 389–393. https://doi.org/10.1038/nature10730.

44. Ramírez, F., Ryan, D.P., Grüning, B., Bhardwaj, V., Kilpert, F., Richter, A.S., Heyne, S., Dündar, F., and Manke, T. (2016). deepTools2: a next generation web server for deep-sequencing data analysis. Nucleic Acids Res. *44*, W160-165. https://doi.org/10.1093/nar/gkw257.

45. Birey, F., Andersen, J., Makinson, C.D., Islam, S., Wei, W., Huber, N., Fan, H.C., Metzler, K.R.C., Panagiotakos, G., Thom, N., et al. (2017). Assembly of functionally integrated human forebrain spheroids. Nature *545*, 54–59. https://doi.org/10.1038/nature22330.

46. Chambers, S.M., Fasano, C.A., Papapetrou, E.P., Tomishima, M., Sadelain, M., and Studer, L. (2009). Highly efficient neural conversion of human ES and iPS cells by dual inhibition of SMAD signaling. Nat. Biotechnol. *27*, 275–280. https://doi.org/10.1038/nbt.1529.

47. Valli, E., Trazzi, S., Fuchs, C., Erriquez, D., Bartesaghi, R., Perini, G., and Ciani, E. (2012). CDKL5, a novel MYCN-repressed gene, blocks cell cycle and promotes differentiation of neuronal cells. Biochim. Biophys. Acta *1819*, 1173–1185. https://doi.org/10.1016/j.bbagrm.2012.08.001.

48. Lecona, E., Rojas, L.A., Bonasio, R., Johnston, A., Fernández-Capetillo, O., and Reinberg, D. (2013). Polycomb protein SCML2 regulates the cell cycle by binding and modulating CDK/CYCLIN/p21 complexes. PLoS Biol. *11*, e1001737. https://doi.org/10.1371/journal.pbio.1001737.

49. Flaherty, E., and Maniatis, T. (2020). The role of clustered protocadherins in neurodevelopment and neuropsychiatric diseases. Curr. Opin. Genet. Dev. *65*, 144–150. https://doi.org/10.1016/j.gde.2020.05.041.

50. Duclot, F., and Kabbaj, M. (2017). The Role of Early Growth Response 1 (EGR1) in Brain Plasticity and Neuropsychiatric Disorders. Front. Behav. Neurosci. *11*, 35. https://doi.org/10.3389/fnbeh.2017.00035.

51. Moreland, T., and Poulain, F.E. (2022). To Stick or Not to Stick: The Multiple Roles of Cell Adhesion Molecules in Neural Circuit Assembly. Front. Neurosci. *16*, 889155. https://doi.org/10.3389/fnins.2022.889155.

52. Steele, J.L., Morrow, M.M., Sarnat, H.B., Alkhunaizi, E., Brandt, T., Chitayat, D.A., DeFilippo, C.P., Douglas, G.V., Dubbs, H.A., Elloumi, H.Z., et al. (2022). Semaphorin-Plexin Signaling: From Axonal Guidance to a New X-Linked Intellectual Disability Syndrome. Pediatr. Neurol. *126*, 65–73. https://doi.org/10.1016/j.pediatrneurol.2021.10.008.

53. Cheng, H.J., Bagri, A., Yaron, A., Stein, E., Pleasure, S.J., and Tessier-Lavigne, M. (2001). Plexin-A3 mediates semaphorin signaling and regulates the development of hippocampal axonal projections. Neuron *32*, 249–263. https://doi.org/10.1016/s0896-6273(01)00478-0.

54. Fogel, B.L., Wexler, E., Wahnich, A., Friedrich, T., Vijayendran, C., Gao, F., Parikshak, N., Konopka, G., and Geschwind, D.H. (2012). RBFOX1 regulates both splicing and transcriptional networks in human neuronal development. Hum. Mol. Genet. *21*, 4171–4186. https://doi.org/10.1093/hmg/dds240.

55. Ou, Jianhong ATACseqTFEA: Transcription Factor Enrichment Analysis for ATAC-seq. Version R package version 1.6.0.

56. Liska, O., Bohár, B., Hidas, A., Korcsmáros, T., Papp, B., Fazekas, D., and Ari, E. (2022). TFLink: an integrated gateway to access transcription factor-target gene

1018 interactions for multiple species. Database J. Biol. Databases Curation *2022*,
1019 baac083. https://doi.org/10.1093/database/baac083.

1020 57. Penisson, M., Ladewig, J., Belvindrah, R., and Francis, F. (2019). Genes and
1021 Mechanisms Involved in the Generation and Amplification of Basal Radial Glial
1022 Cells. Front. Cell. Neurosci. *13*, 381. https://doi.org/10.3389/fncel.2019.00381.

1023 58. Lynch, D.C., Revil, T., Schwartzentruber, J., Bhoj, E.J., Innes, A.M., Lamont, R.E.,
1024 Lemire, E.G., Chodirker, B.N., Taylor, J.P., Zackai, E.H., et al. (2014). Disrupted
1025 auto-regulation of the spliceosomal gene SNRPB causes cerebro-costo-mandibular
1026 syndrome. Nat. Commun. *5*, 4483. https://doi.org/10.1038/ncomms5483.

1027 59. Lewis, P.W., Müller, M.M., Koletsky, M.S., Cordero, F., Lin, S., Banaszynski, L.A.,
1028 Garcia, B.A., Muir, T.W., Becher, O.J., and Allis, C.D. (2013). Inhibition of PRC2
1029 activity by a gain-of-function H3 mutation found in pediatric glioblastoma. Science
1030 *340*, 857–861. https://doi.org/10.1126/science.1232245.

1031 60. Shi, L., Shi, J., Shi, X., Li, W., and Wen, H. (2018). Histone H3.3 G34 Mutations Alter
1032 Histone H3K36 and H3K27 Methylation In Cis. J. Mol. Biol. *430*, 1562–1565.
1033 https://doi.org/10.1016/j.jmb.2018.04.014.

1034 61. Parenti, I., Rabaneda, L.G., Schoen, H., and Novarino, G. (2020).
1035 Neurodevelopmental Disorders: From Genetics to Functional Pathways. Trends
1036 Neurosci. *43*, 608–621. https://doi.org/10.1016/j.tins.2020.05.004.

1037 62. Shah, P.S., Weksberg, R., and Chitayat, D. (2006). Overgrowth with severe
1038 developmental delay following IVF/ICSI: A newly recognized syndrome? Am. J. Med.
1039 Genet. A. *140*, 1312–1315. https://doi.org/10.1002/ajmg.a.31274.

1040 63. Wenzel, T.J., and Mousseau, D.D. (2024). Brain organoids engineered to give rise to
1041 glia and neural networks after 90 days in culture exhibit human-specific proteoforms.
1042 Front. Cell. Neurosci. *18*, 1383688. https://doi.org/10.3389/fncel.2024.1383688.

1043 64. Mulder, L.A., Depla, J.A., Sridhar, A., Wolthers, K., Pajkrt, D., and Vieira de Sá, R.
1044 (2023). A beginner's guide on the use of brain organoids for neuroscientists: a
1045 systematic review. Stem Cell Res. Ther. *14*, 87. https://doi.org/10.1186/s13287-023-
1046 03302-x.

1047 65. James, O.G., Selvaraj, B.T., Magnani, D., Burr, K., Connick, P., Barton, S.K.,
1048 Vasistha, N.A., Hampton, D.W., Story, D., Smigiel, R., et al. (2021). iPSC-derived
1049 myelinoids to study myelin biology of humans. Dev. Cell *56*, 1346-1358.e6.
1050 https://doi.org/10.1016/j.devcel.2021.04.006.

1051 66. Fasipe, O.J., Agede, O.A., and Enikuomehin, A.C. (2020). Announcing the novel
1052 class of GABA-A receptor selective positive allosteric modulator antidepressants.
1053 Future Sci. OA *7*, FSO654. https://doi.org/10.2144/fsoa-2020-0108.

1054 67. Bankhead, P., Loughrey, M.B., Fernández, J.A., Dombrowski, Y., McArt, D.G.,
1055 Dunne, P.D., McQuaid, S., Gray, R.T., Murray, L.J., Coleman, H.G., et al. (2017).
1056 QuPath: Open source software for digital pathology image analysis. Sci. Rep. *7*,
1057 16878. https://doi.org/10.1038/s41598-017-17204-5.

1058 68. Takeichi, M. (2007). The cadherin superfamily in neuronal connections and
1059 interactions. Nat. Rev. Neurosci. *8*, 11–20. https://doi.org/10.1038/nrn2043.

1060 69. Polanco, J., Reyes-Vigil, F., Weisberg, S.D., Dhimitruka, I., and Brusés, J.L. (2021).
1061 Differential Spatiotemporal Expression of Type I and Type II Cadherins Associated
1062 With the Segmentation of the Central Nervous System and Formation of Brain
1063 Nuclei in the Developing Mouse. Front. Mol. Neurosci. *14*, 633719.
1064 https://doi.org/10.3389/fnmol.2021.633719.

1065 70. Kiefel, H., Bondong, S., Hazin, J., Ridinger, J., Schirmer, U., Riedle, S., and Altevogt,
1066 P. (2012). L1CAM: a major driver for tumor cell invasion and motility. Cell Adhes.
1067 Migr. *6*, 374–384. https://doi.org/10.4161/cam.20832.

1068 71. Robertson, S.P., Twigg, S.R.F., Sutherland-Smith, A.J., Biancalana, V., Gorlin, R.J.,
1069 Horn, D., Kenwrick, S.J., Kim, C.A., Morava, E., Newbury-Ecob, R., et al. (2003).
1070 Localized mutations in the gene encoding the cytoskeletal protein filamin A cause
1071 diverse malformations in humans. Nat. Genet. *33*, 487–491.
1072 https://doi.org/10.1038/ng1119.

1073 72. Feng, Y., Chen, M.H., Moskowitz, I.P., Mendonza, A.M., Vidali, L., Nakamura, F.,
1074 Kwiatkowski, D.J., and Walsh, C.A. (2006). Filamin A (FLNA) is required for cell-cell
1075 contact in vascular development and cardiac morphogenesis. Proc. Natl. Acad. Sci.
1076 U. S. A. *103*, 19836–19841. https://doi.org/10.1073/pnas.0609628104.

1077 73. Ciani, L., Boyle, K.A., Dickins, E., Sahores, M., Anane, D., Lopes, D.M., Gibb, A.J.,
1078 and Salinas, P.C. (2011). Wnt7a signaling promotes dendritic spine growth and
1079 synaptic strength through Ca^{2+}/Calmodulin-dependent protein kinase II. Proc. Natl.
1080 Acad. Sci. U. S. A. *108*, 10732–10737. https://doi.org/10.1073/pnas.1018132108.

1081 74. Caracci, M.O., Avila, M.E., Espinoza-Cavieres, F.A., López, H.R., Ugarte, G.D., and
1082 De Ferrari, G.V. (2021). Wnt/β-Catenin-Dependent Transcription in Autism Spectrum
1083 Disorders. Front. Mol. Neurosci. *14*, 764756.
1084 https://doi.org/10.3389/fnmol.2021.764756.

1085 75. Qu, Q., Sun, G., Murai, K., Ye, P., Li, W., Asuelime, G., Cheung, Y.-T., and Shi, Y.
1086 (2013). Wnt7a regulates multiple steps of neurogenesis. Mol. Cell. Biol. *33*, 2551–
1087 2559. https://doi.org/10.1128/MCB.00325-13.

1088 76. Vogt, D.L., Gray, C.D., Young, W.S., Orellana, S.A., and Malouf, A.T. (2007).
1089 ARHGAP4 is a novel RhoGAP that mediates inhibition of cell motility and axon
1090 outgrowth. Mol. Cell. Neurosci. *36*, 332–342.
1091 https://doi.org/10.1016/j.mcn.2007.07.004.

1092 77. Duan, Y., Wang, S.-H., Song, J., Mironova, Y., Ming, G., Kolodkin, A.L., and Giger,
1093 R.J. (2014). Semaphorin 5A inhibits synaptogenesis in early postnatal- and adult-
1094 born hippocampal dentate granule cells. eLife *3*, e04390.
1095 https://doi.org/10.7554/eLife.04390.

1096 78. Grebbin, B.M., Hau, A.-C., Groß, A., Anders-Maurer, M., Schramm, J., Koss, M.,
1097 Wille, C., Mittelbronn, M., Selleri, L., and Schulte, D. (2016). Pbx1 is required for
1098 adult subventricular zone neurogenesis. Dev. Camb. Engl. *143*, 2281–2291.
1099 https://doi.org/10.1242/dev.128033.

1100 79. Villaescusa, J.C., Li, B., Toledo, E.M., Rivetti di Val Cervo, P., Yang, S., Stott, S.R.,
1101 Kaiser, K., Islam, S., Gyllborg, D., Laguna-Goya, R., et al. (2016). A PBX1
1102 transcriptional network controls dopaminergic neuron development and is impaired
1103 in Parkinson's disease. EMBO J. *35*, 1963–1978.
1104 https://doi.org/10.15252/embj.201593725.

1105 80. Colasante, G., Collombat, P., Raimondi, V., Bonanomi, D., Ferrai, C., Maira, M.,
1106 Yoshikawa, K., Mansouri, A., Valtorta, F., Rubenstein, J.L.R., et al. (2008). Arx is a
1107 direct target of Dlx2 and thereby contributes to the tangential migration of
1108 GABAergic interneurons. J. Neurosci. Off. J. Soc. Neurosci. *28*, 10674–10686.
1109 https://doi.org/10.1523/JNEUROSCI.1283-08.2008.

1110 81. Lim, Y., Cho, I.-T., Shi, X., Grinspan, J.B., Cho, G., and Golden, J.A. (2019). Arx
1111 Expression Suppresses Ventralization of the Developing Dorsal Forebrain. Sci. Rep.
1112 *9*, 226. https://doi.org/10.1038/s41598-018-36194-6.

1113 82. Jacobs, W.B., Govoni, G., Ho, D., Atwal, J.K., Barnabe-Heider, F., Keyes, W.M.,
1114 Mills, A.A., Miller, F.D., and Kaplan, D.R. (2005). p63 is an essential proapoptotic
1115 protein during neural development. Neuron *48*, 743–756.
1116 https://doi.org/10.1016/j.neuron.2005.10.027.

1117 83. Bishop, K.M., Rubenstein, J.L.R., and O'Leary, D.D.M. (2002). Distinct actions of
1118 Emx1, Emx2, and Pax6 in regulating the specification of areas in the developing
1119 neocortex. J. Neurosci. Off. J. Soc. Neurosci. *22*, 7627–7638.
1120 https://doi.org/10.1523/JNEUROSCI.22-17-07627.2002.

1121 84. Lin, L., Sun, W., Throesch, B., Kung, F., Decoster, J.T., Berner, C.J., Cheney, R.E.,
1122 Rudy, B., and Hoffman, D.A. (2013). DPP6 regulation of dendritic morphogenesis
1123 impacts hippocampal synaptic development. Nat. Commun. *4*, 2270.
1124 https://doi.org/10.1038/ncomms3270.

1125 85. Malloy, C., Ahern, M., Lin, L., and Hoffman, D.A. (2022). Neuronal Roles of the
1126 Multifunctional Protein Dipeptidyl Peptidase-like 6 (DPP6). Int. J. Mol. Sci. *23*, 9184.
1127 https://doi.org/10.3390/ijms23169184.

1128 86. Naujock, M., Speidel, A., Fischer, S., Kizner, V., Dorner-Ciossek, C., and Gillardon,
1129 F. (2020). Neuronal Differentiation of Induced Pluripotent Stem Cells from
1130 Schizophrenia Patients in Two-Dimensional and in Three-Dimensional Cultures

Reveals Increased Expression of the Kv4.2 Subunit DPP6 That Contributes to Decreased Neuronal Activity. Stem Cells Dev. *29*, 1577–1587. https://doi.org/10.1089/scd.2020.0082.

87. Karayannis, T., Au, E., Patel, J.C., Kruglikov, I., Markx, S., Delorme, R., Héron, D., Salomon, D., Glessner, J., Restituito, S., et al. (2014). Cntnap4 differentially contributes to GABAergic and dopaminergic synaptic transmission. Nature *511*, 236–240. https://doi.org/10.1038/nature13248.

88. Young, S.Z., Lafourcade, C.A., Platel, J.-C., Lin, T.V., and Bordey, A. (2014). GABAergic striatal neurons project dendrites and axons into the postnatal subventricular zone leading to calcium activity. Front. Cell. Neurosci. *8*, 10. https://doi.org/10.3389/fncel.2014.00010.

89. Hotz, A.L., Jamali, A., Rieser, N.N., Niklaus, S., Aydin, E., Myren-Svelstad, S., Lalla, L., Jurisch-Yaksi, N., Yaksi, E., and Neuhauss, S.C.F. (2022). Loss of glutamate transporter eaat2a leads to aberrant neuronal excitability, recurrent epileptic seizures, and basal hypoactivity. Glia *70*, 196–214. https://doi.org/10.1002/glia.24106.

90. Rylaarsdam, L., Rakotomamonjy, J., Pope, E., and Guemez-Gamboa, A. (2024). iPSC-derived models of PACS1 syndrome reveal transcriptional and functional deficits in neuron activity. Nat. Commun. *15*, 827. https://doi.org/10.1038/s41467-024-44989-7.

91. Butler, K.M., Moody, O.A., Schuler, E., Coryell, J., Alexander, J.J., Jenkins, A., and Escayg, A. (2018). De novo variants in GABRA2 and GABRA5 alter receptor function and contribute to early-onset epilepsy. Brain J. Neurol. *141*, 2392–2405. https://doi.org/10.1093/brain/awy171.

92. Kim, S., Kim, H., and Um, J.W. (2018). Synapse development organized by neuronal activity-regulated immediate-early genes. Exp. Mol. Med. *50*, 1–7. https://doi.org/10.1038/s12276-018-0025-1.

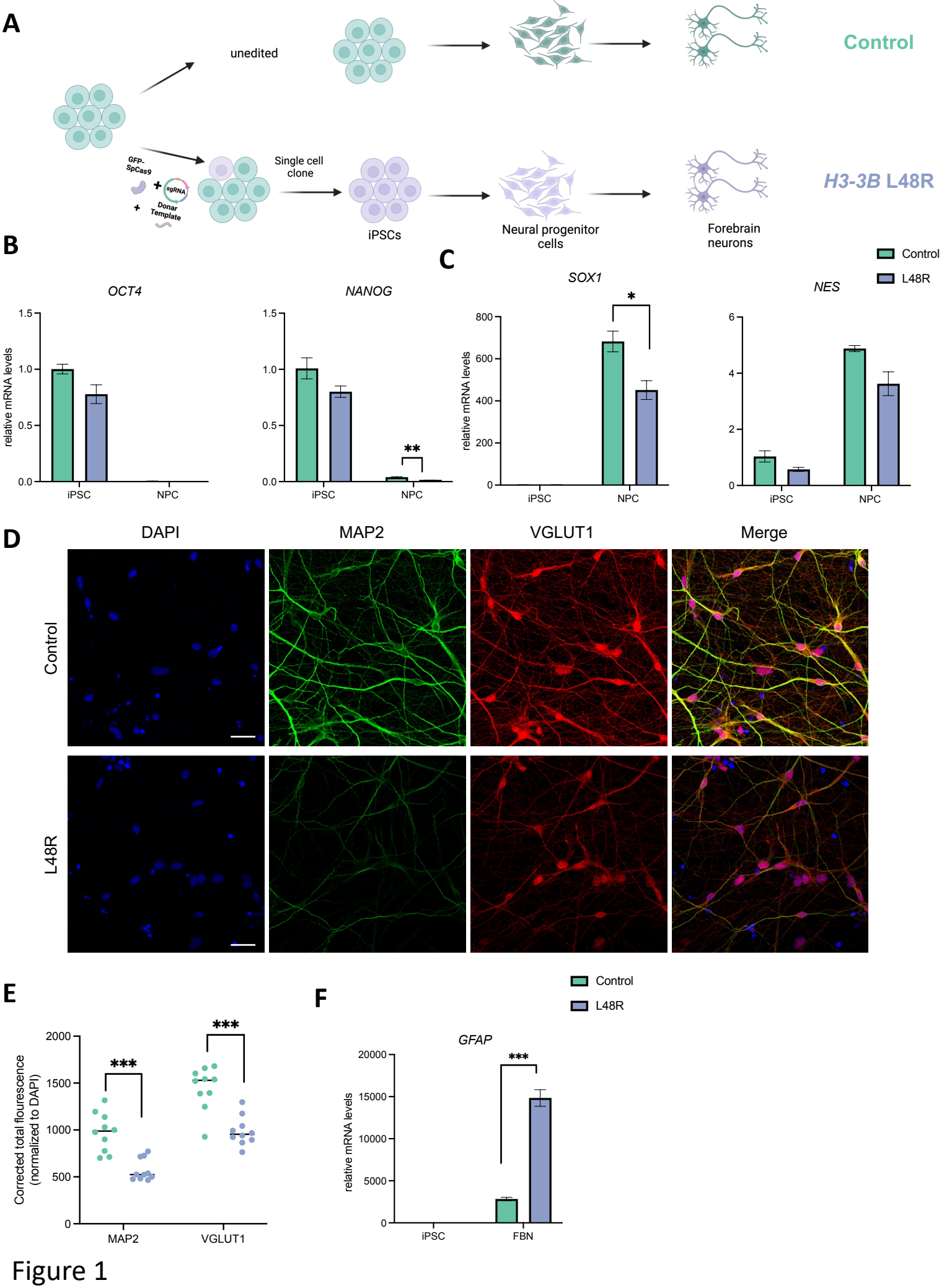
A
unedited
Control
GFP-SpCas9
sgRNA
Donar Template
Single cell clone
iPSCs
Neural progenitor cells
Forebrain neurons
H3-3B L48R
B
OCT4
NANOG
relative mRNA levels
iPSC
NPC
**
C
Control
L48R
SOX1
NES
*
D
DAPI
MAP2
VGLUT1
Merge
Control
L48R
E
Corrected total flourescence (normalized to DAPI)
***
MAP2
VGLUT1
F
GFAP
relative mRNA levels
iPSC
FBN

Figure 1

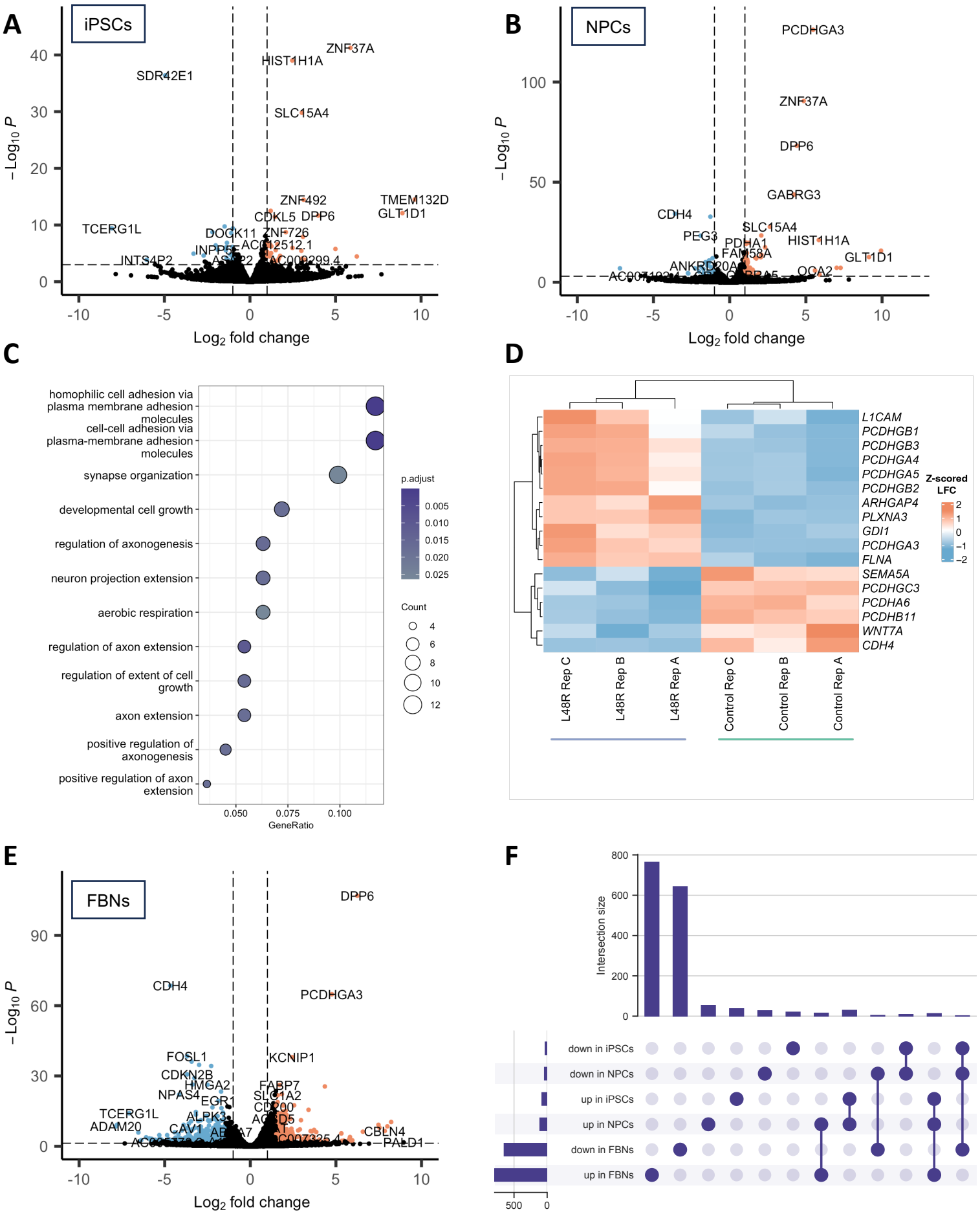
A
iPSCs
SDR42E1
HIST1H1A
ZNF37A
SLC15A4
ZNF492
TMEM132D
GLT1D1
CDKL5
DPP6
TCERG1L
DOCK11
ZNF726
INPP5E
AC012512.1
INTS4P2
AC009299.4
−Log10 P
Log2 fold change
B
NPCs
PCDHGA3
ZNF37A
DPP6
GABRG3
CDH4
SLC15A4
PEG3
PDHA1
HIST1H1A
FAM58A
GLT1D1
ANKRD20A
OCA2
−Log10 P
Log2 fold change
C
homophilic cell adhesion via plasma membrane adhesion molecules
cell-cell adhesion via plasma-membrane adhesion molecules
synapse organization
developmental cell growth
regulation of axonogenesis
neuron projection extension
aerobic respiration
regulation of axon extension
regulation of extent of cell growth
axon extension
positive regulation of axonogenesis
positive regulation of axon extension
GeneRatio
p.adjust
Count
D
L1CAM
PCDHGB1
PCDHGB3
PCDHGA4
PCDHGA5
PCDHGB2
ARHGAP4
PLXNA3
GDI1
PCDHGA3
FLNA
SEMA5A
PCDHGC3
PCDHA6
PCDHB11
WNT7A
CDH4
Z-scored LFC
L48R Rep C
L48R Rep B
L48R Rep A
Control Rep C
Control Rep B
Control Rep A
E
FBNs
DPP6
CDH4
PCDHGA3
FOSL1
KCNIP1
CDKN2B
HMGA2
FABP7
NPAS4
EGR1
SLC1A2
TCERG1L
ALPK3
ADAM20
CAV1
CBLN4
PALD1
−Log10 P
Log2 fold change
F
Intersection size
down in iPSCs
down in NPCs
up in iPSCs
up in NPCs
down in FBNs
up in FBNs

Figure 2

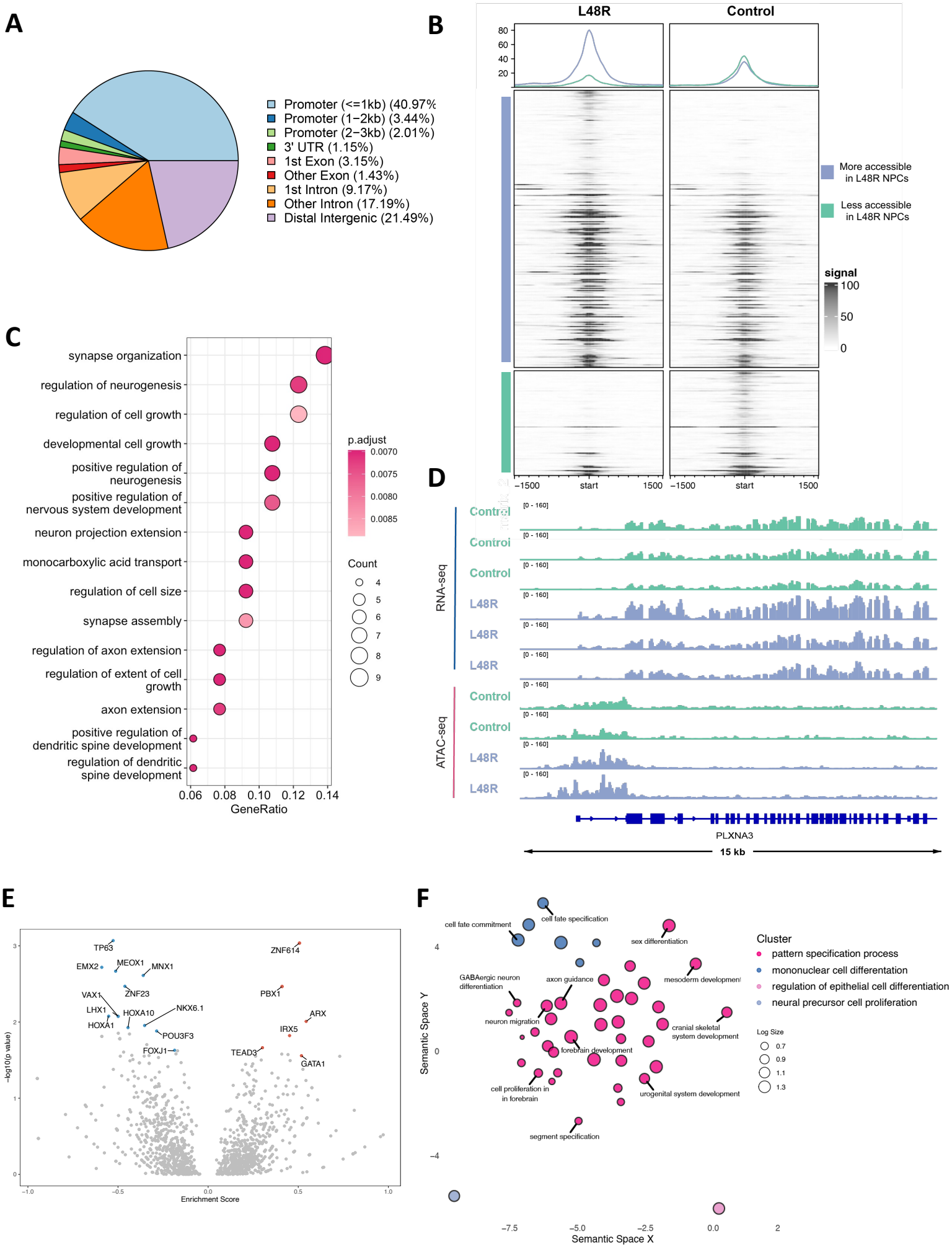
A
Promoter (<=1kb) (40.97%
Promoter (1−2kb) (3.44%)
Promoter (2−3kb) (2.01%)
3' UTR (1.15%)
1st Exon (3.15%)
Other Exon (1.43%)
1st Intron (9.17%)
Other Intron (17.19%)
Distal Intergenic (21.49%)
B
L48R
Control
More accessible in L48R NPCs
Less accessible in L48R NPCs
signal
100
50
0
−1500
start
1500
C
synapse organization
regulation of neurogenesis
regulation of cell growth
developmental cell growth
positive regulation of neurogenesis
positive regulation of nervous system development
neuron projection extension
monocarboxylic acid transport
regulation of cell size
synapse assembly
regulation of axon extension
regulation of extent of cell growth
axon extension
positive regulation of dendritic spine development
regulation of dendritic spine development
0.06
0.08
0.10
0.12
0.14
GeneRatio
p.adjust
0.0070
0.0075
0.0080
0.0085
Count
4
5
6
7
8
9
D
RNA-seq
ATAC-seq
Control
L48R
[0 - 160]
PLXNA3
15 kb
E
TP63
EMX2
MEOX1
MNX1
ZNF614
VAX1
ZNF23
PBX1
LHX1
HOXA10
NKX6.1
ARX
HOXA1
IRX5
POU3F3
FOXJ1
TEAD3
GATA1
−log10(p value)
Enrichment Score
F
cell fate commitment
cell fate specification
sex differentiation
GABAergic neuron differentiation
axon guidance
mesoderm development
neuron migration
cranial skeletal system development
forebrain development
cell proliferation in in forebrain
urogenital system development
segment specification
Semantic Space Y
Semantic Space X
Cluster
pattern specification process
mononuclear cell differentiation
regulation of epithelial cell differentiation
neural precursor cell proliferation
Log Size
0.7
0.9
1.1
1.3

Figure 3

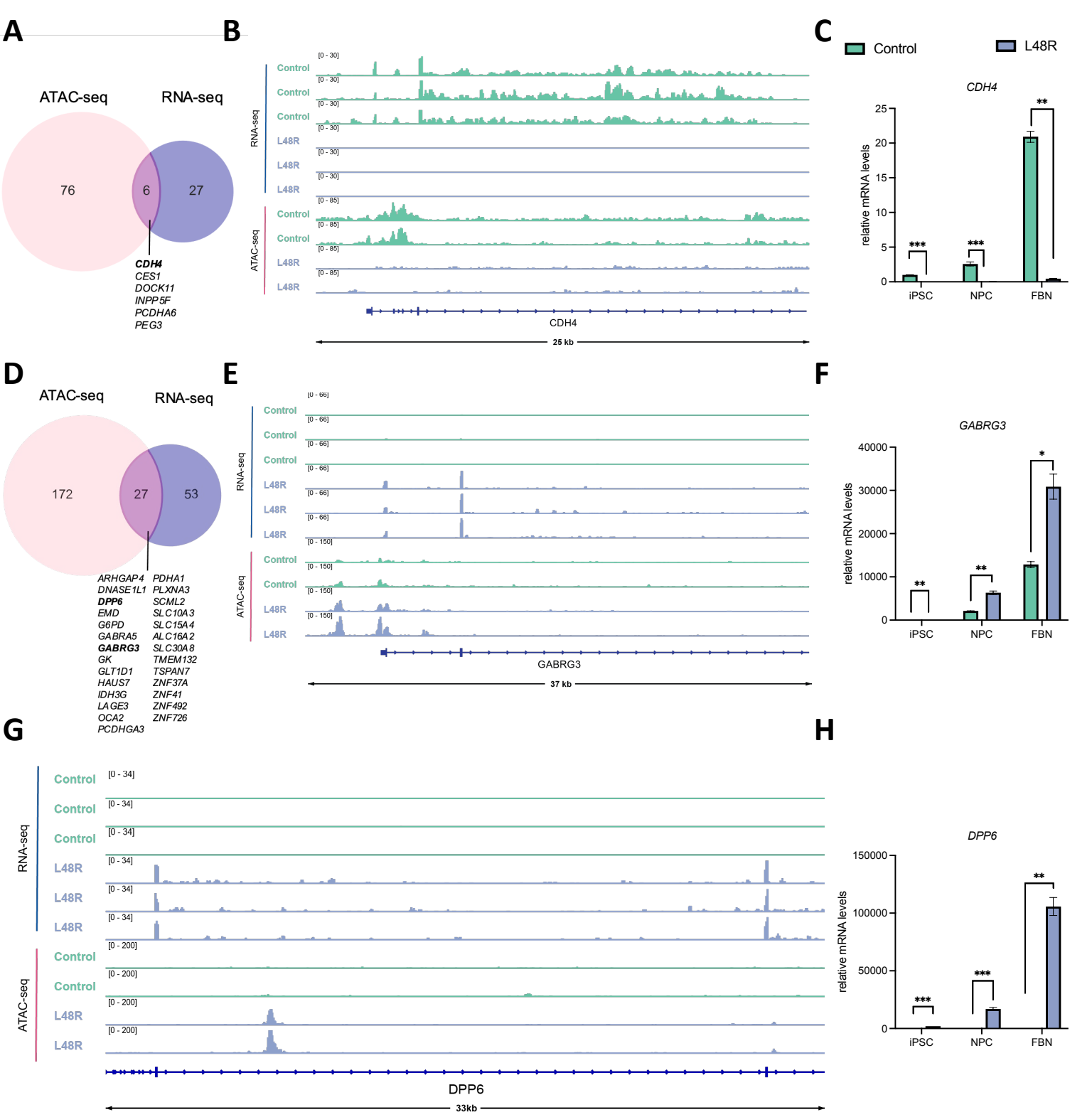
A
ATAC-seq
RNA-seq
76
6
27
CDH4
CES1
DOCK11
INPP5F
PCDHA6
PEG3
B
RNA-seq
ATAC-seq
Control
L48R
CDH4
25 kb
C
Control
L48R
CDH4
relative mRNA levels
iPSC
NPC
FBN
D
ATAC-seq
RNA-seq
172
27
53
ARHGAP4
DNASE1L1
DPP6
EMD
G6PD
GABRA5
GABRG3
GK
GLT1D1
HAUS7
IDH3G
LAGE3
OCA2
PCDHGA3
PDHA1
PLXNA3
SCML2
SLC10A3
SLC15A4
ALC16A2
SLC30A8
TMEM132
TSPAN7
ZNF37A
ZNF41
ZNF492
ZNF726
E
GABRG3
37 kb
F
GABRG3
G
DPP6
33kb
H
DPP6

Figure 4

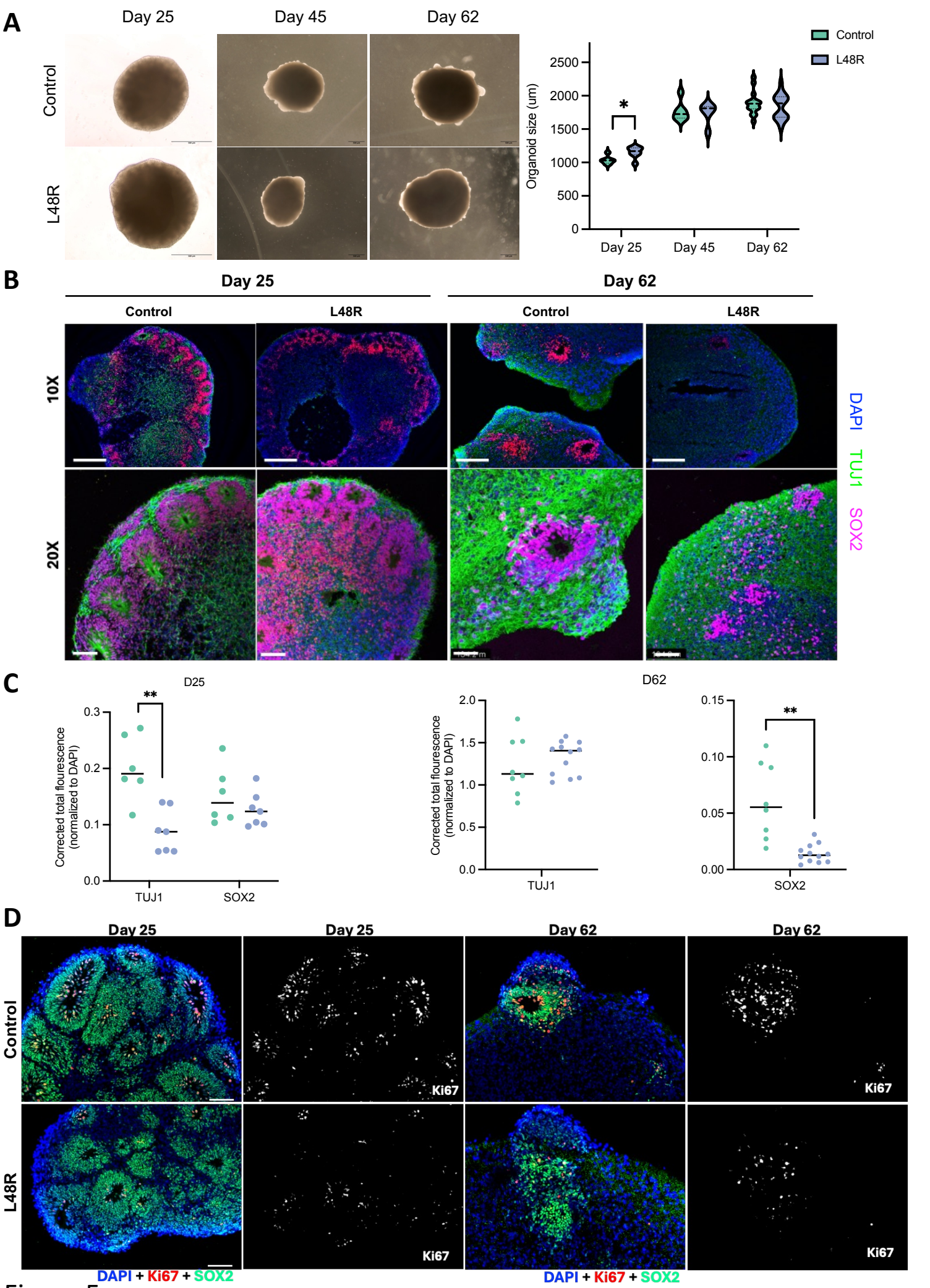
A
Day 25
Day 45
Day 62
Control
L48R
Control
L48R
Organoid size (um)
2500
2000
1500
1000
500
0
*
Day 25
Day 45
Day 62
B
Day 25
Day 62
Control
L48R
Control
L48R
10X
20X
DAPI
TUJ1
SOX2
C
D25
D62
Corrected total flourescence (normalized to DAPI)
0.3
0.2
0.1
0.0
**
TUJ1
SOX2
2.0
1.5
1.0
0.5
0.0
TUJ1
0.15
0.10
0.05
0.00
**
SOX2
D
Day 25
Day 25
Day 62
Day 62
Control
L48R
Ki67
Ki67
Ki67
Ki67
DAPI + Ki67 + SOX2
DAPI + Ki67 + SOX2

Figure 5

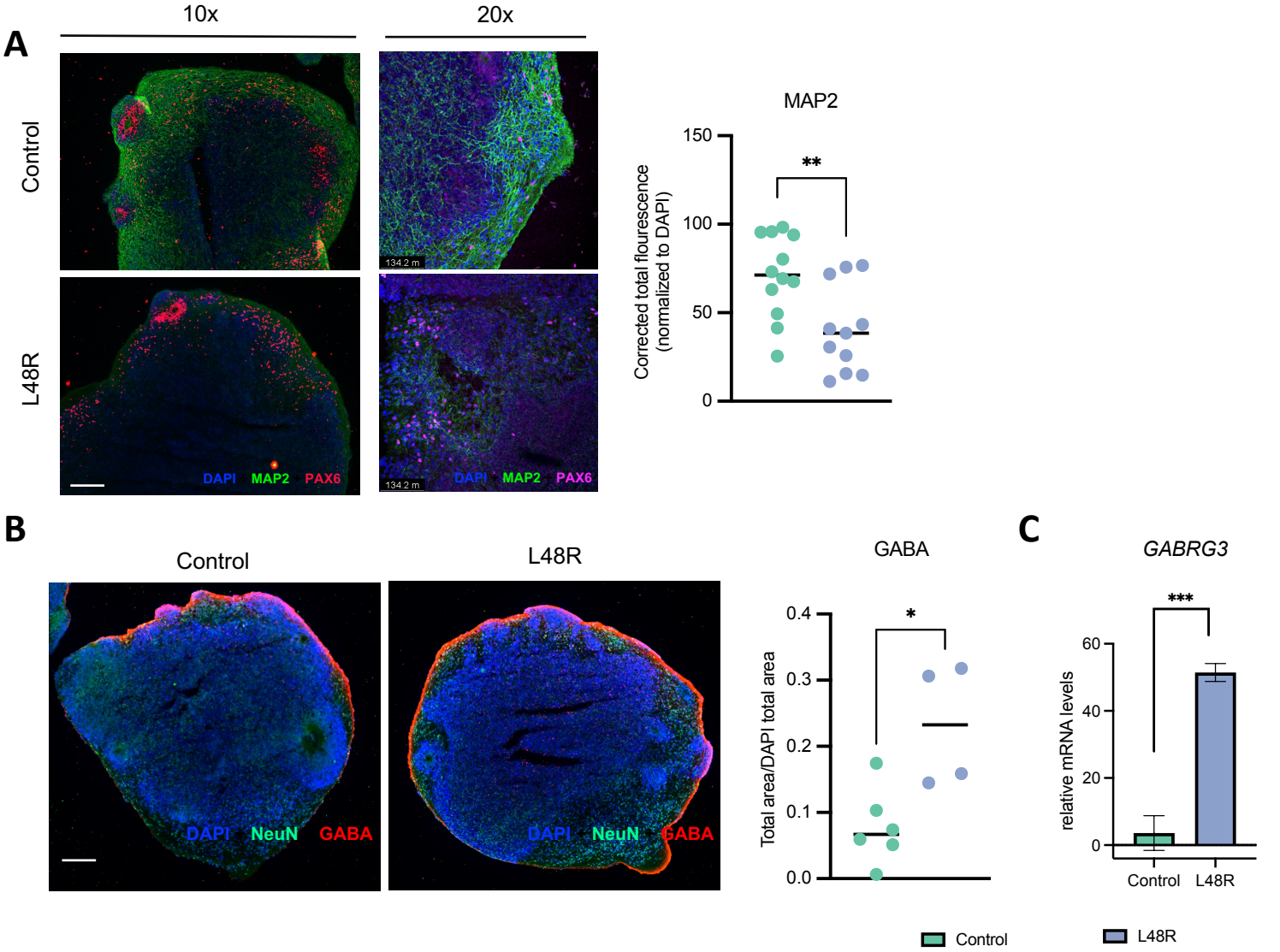
A
10x
20x
Control
L48R
DAPI MAP2 PAX6
MAP2
Corrected total flourescence (normalized to DAPI)
150
100
50
0
**
B
Control
L48R
DAPI NeuN GABA
GABA
Total area/DAPI total area
0.4
0.3
0.2
0.1
0.0
*
C
GABRG3
relative mRNA levels
60
40
20
0
***
Control
L48R

Figure 6

A

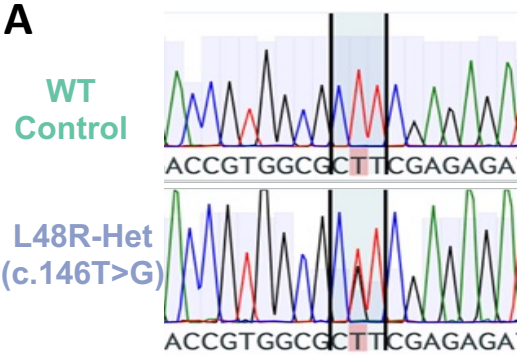

B

Donor Ethnicity	Method	Cell	Age	Sex	Karyotype	CNVs
Hispanic	Sendai	PBMC	Adult	F	Normal	- 0.3 Mb dup 2q24 (DAPL1, TANC1) - 0.2 Mb del 4q32 (no coding genes detected) - 0.3 Mb del 21p11 (no coding genes detected)

C

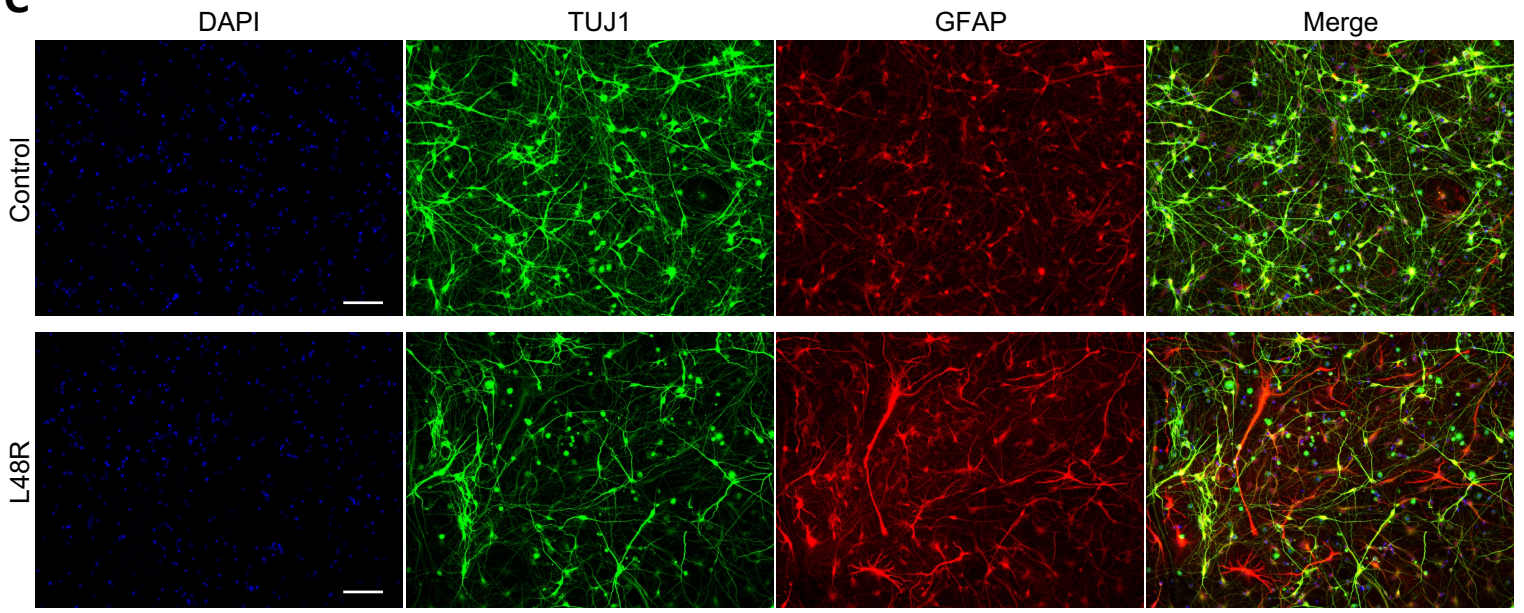

D

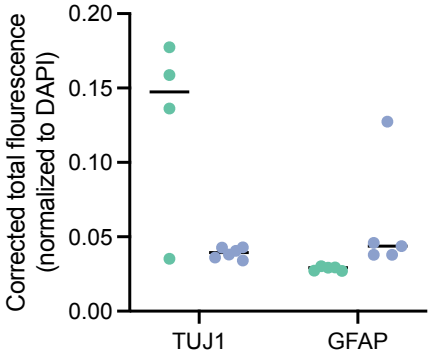

E

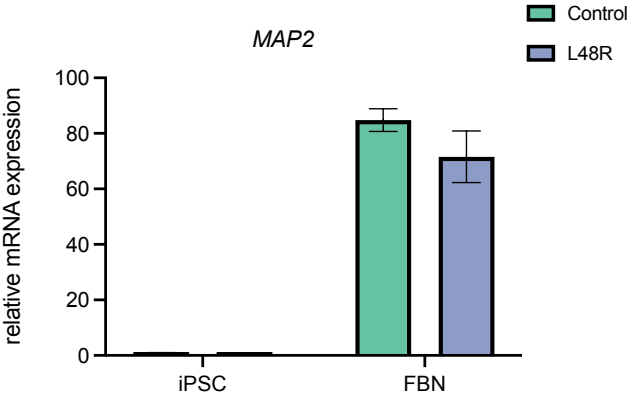

Figure S1

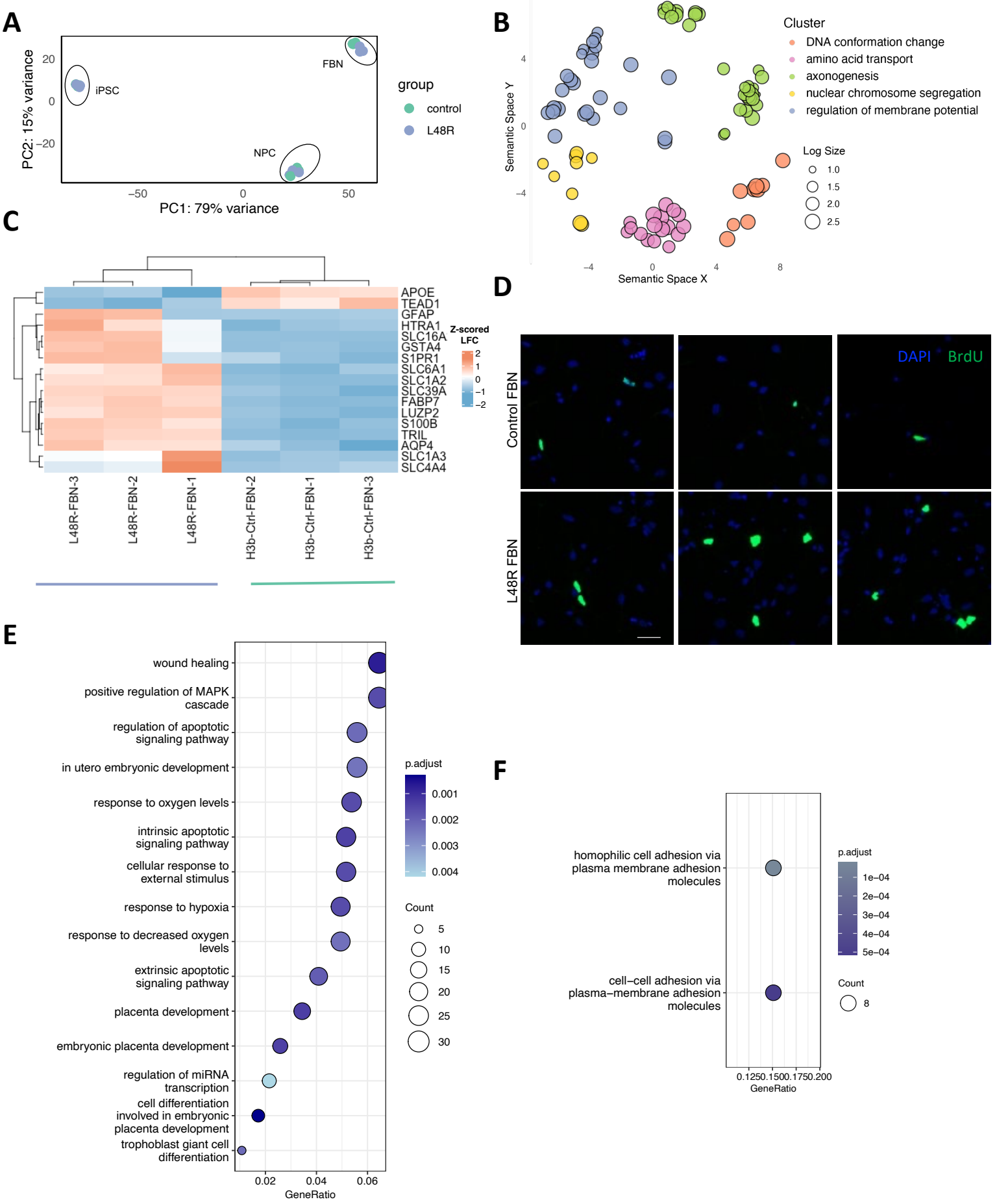
A
PC2: 15% variance
PC1: 79% variance
iPSC
FBN
NPC
group
control
L48R
B
Cluster
DNA conformation change
amino acid transport
axonogenesis
nuclear chromosome segregation
regulation of membrane potential
Log Size
Semantic Space X
Semantic Space Y
C
Z-scored LFC
APOE
TEAD1
GFAP
HTRA1
SLC16A
GSTA4
S1PR1
SLC6A1
SLC1A2
SLC39A
FABP7
LUZP2
S100B
TRIL
AQP4
SLC1A3
SLC4A4
L48R-FBN-3
L48R-FBN-2
L48R-FBN-1
H3b-Ctrl-FBN-2
H3b-Ctrl-FBN-1
H3b-Ctrl-FBN-3
D
DAPI
BrdU
Control FBN
L48R FBN
E
wound healing
positive regulation of MAPK cascade
regulation of apoptotic signaling pathway
in utero embryonic development
response to oxygen levels
intrinsic apoptotic signaling pathway
cellular response to external stimulus
response to hypoxia
response to decreased oxygen levels
extrinsic apoptotic signaling pathway
placenta development
embryonic placenta development
regulation of miRNA transcription
cell differentiation involved in embryonic placenta development
trophoblast giant cell differentiation
GeneRatio
p.adjust
Count
F
homophilic cell adhesion via plasma membrane adhesion molecules
cell–cell adhesion via plasma–membrane adhesion molecules
GeneRatio
p.adjust
Count

Figure S2

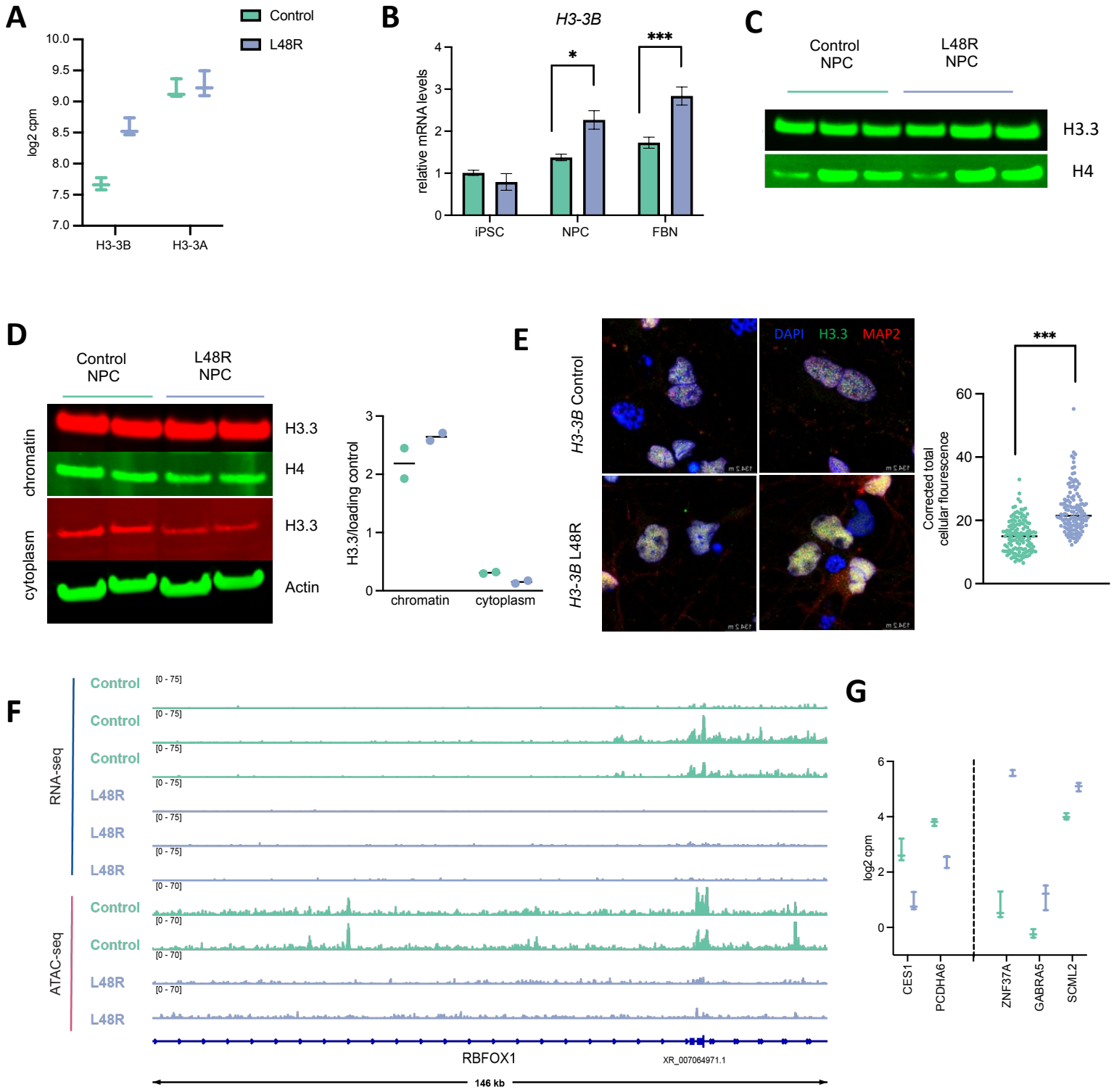
A
Control
L48R
log2 cpm
10.0
9.5
9.0
8.5
8.0
7.5
7.0
H3-3B
H3-3A
B
H3-3B
relative mRNA levels
*
***
iPSC
NPC
FBN
C
Control NPC
L48R NPC
H3.3
H4
D
Control NPC
L48R NPC
chromatin
cytoplasm
H3.3
H4
H3.3
Actin
H3.3/loading control
chromatin
cytoplasm
E
H3-3B Control
H3-3B L48R
DAPI H3.3 MAP2
***
Corrected total cellular flourescence
F
RNA-seq
ATAC-seq
Control
L48R
[0 - 75]
[0 - 70]
RBFOX1
XR_007064971.1
146 kb
G
log2 cpm
CES1
PCDHA6
ZNF37A
GABRA5
SCML2

Figure S3

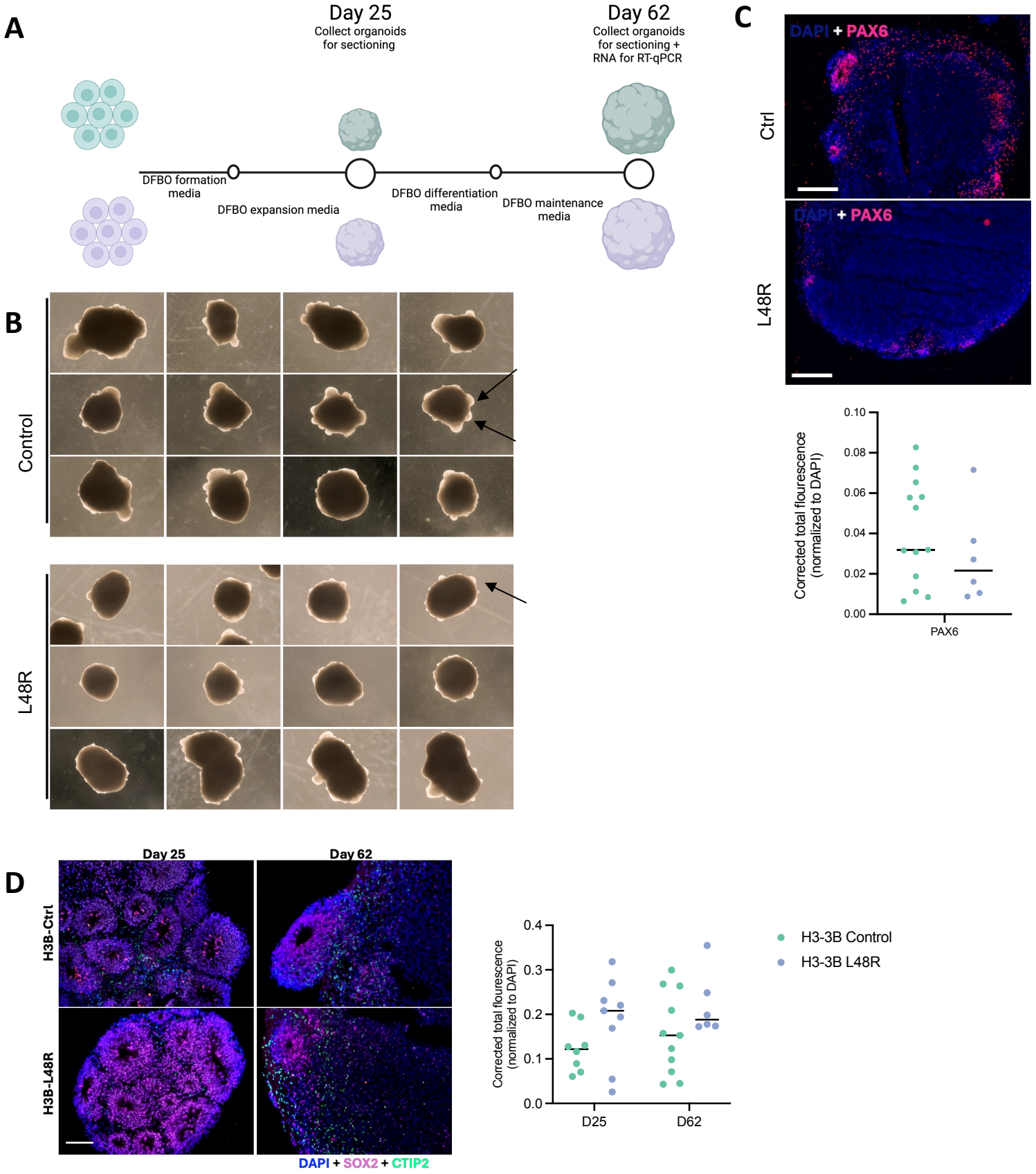
A
Day 25
Collect organoids for sectioning
Day 62
Collect organoids for sectioning + RNA for RT-qPCR
DFBO formation media
DFBO expansion media
DFBO differentiation media
DFBO maintenance media
B
Control
L48R
C
Ctrl
L48R
DAPI + PAX6
Corrected total flourescence (normalized to DAPI)
0.10
0.08
0.06
0.04
0.02
0.00
PAX6
D
Day 25
Day 62
H3B-Ctrl
H3B-L48R
DAPI + SOX2 + CTIP2
Corrected total flourescence (normalized to DAPI)
0.4
0.3
0.2
0.1
0.0
D25
D62
H3-3B Control
H3-3B L48R

Figure S4